This peer-reviewed article has been accepted for publication in Publications of the Astronomical Society of Australia but not yet copyedited or typeset, and so may be subject to change during the production process.

The article is considered published and may be cited using its DOI. 10.1017/pasa.2026.10229

The Southern-sky MWA Rapid Two-metre (SMART) pulsar survey—IV. Survey update and an atlas of 205 non-recycled southern pulsars

N. D. R. Bhat,[1] C. P. Lee,[1] S. J. McSweeney,[1,2] B. W. Meyers,[3,1] C. M. Tan,[1] M. Xue,[4] Qiuyang Fu,[4] N. A. Swainston,[1,5] S. M. Ord,[6] G. J. Sleap,[1] S. E. Tremblay,[7] W. van Straten,[8] A. Williams,[1] C. Di Pientrantonio,[9] C. J. Harris,[9] and P. J. Elahi[9]

[1]International Centre for Radio Astronomy Research, Curtin University, Bentley, WA 6102, Australia
[2]SKA Observatory, SKA-Low Science Operations Centre, 26 Dick Perry Avenue, Kensington, WA 6151, Australia
[3]Australian SKA Regional Centre (AusSRC), Curtin University, Kent Street, Bentley, WA 6102, Australia
[4]National Astronomical Observatories, Chinese Academy of Sciences, Datun Road, Chaoyang District, Beijing 100101, China
[5]CSIRO Space and Astronomy, PO Box 1130, Bentley, WA 6102, Australia
[6]CSIRO Astronomy and Space Science, PO Box 76, Epping, NSW 1710, Australia
[7]National Radio Astronomy Observatory, 1011 Lopezville Road, Socorro, NM 87801, USA
[8] Manly Astrophysics, 15/41-42 East Esplanade, Manly, NSW 2095, Australia
[9]Pawsey Supercomputing Research Centre, Kensington, WA 6151, Australia

Abstract

The Southern-sky MWA Rapid Two-metre (SMART) survey, which capitalises on the MWA's large field of view and voltage recording capability, is an ambitious effort to conduct sensitive searches for pulsars and fast transients in the 140–170 MHz band. The novelty of voltage recording, long dwell times (4800 s) and the high-time and -frequency resolutions (100 µs/10-kHz) exchange a large survey speed ($\sim 450\,\mathrm{deg}^2\,\mathrm{h}^{-1}$) for high computational cost. The survey covers the entire sky south of +30° in declination through a series of dedicated observing campaigns, accumulating nearly four petabytes of data. The large volumes of data and the processing challenges at low frequencies necessitate data processing to be approached in multiple phases, and the initial searches focused on a first-pass (shallow) survey of parts of the skies, as reported in earlier papers in this series. These data are also processed for re-detections of hundreds of known pulsars in the southern sky, many of which are also the first detections at frequencies below 400 MHz. This paper is motivated by the need to address the inherent difficulties (for the wider community) in handling large amounts of voltage data and software/processing challenges for routine pulsar detections, and also by the fast-evolving landscape of the SKA Observatory (SKAO). With the construction and commissioning ramping up towards the full-scale SKA-Low, a low-frequency catalogue of detectable pulsars in the southern sky will prove to be a valuable reference for the science verification exercise. A growing sample of low-frequency pulsar detections and measurements will also prove invaluable in a variety of science applications including population studies, survey simulations and emission beam models, refining interstellar medium models for electron densities and the spatial distribution of turbulence, and also for forecasting the detection prospects and survey yield from pulsar surveys planned with SKA-Low. We also present an electronic catalogue of various data products, including pulse profiles, time series and multi-channel folded archives, along with the measurements of dispersion and rotation measures, and mean flux densities for the detected pulsars, and this will be periodically updated as more detections flow on from the ongoing data processing.

Keywords: surveys: sky surveys – instrumentation: interferometers — methods: observational –- pulsars: general – techniques: interferometric

1. Introduction

The Southern-sky MWA Rapid Two-metre (SMART) survey is an ambitious effort that leverages the Voltage Capture System (VCS) and large field-of-view (FoV) of the Murchison Widefield Array (MWA; Tingay et al. 2013; Wayth et al. 2018) to undertake an all-sky survey for pulsars and fast transients in the 140–170 MHz band. It is the first large-scale pulsar survey in the southern sky in the frequency band of the low-frequency component of the SKAO (SKA-Low; 50–350 MHz). With its long dwell times (4800 s) and high-time and -frequency resolutions (100 µs/10 kHz), the SMART survey will be much more sensitive than previous-generation southern-sky pulsar surveys (e.g., Manchester et al. 1996; Manchester et al. 2001; Keith et al. 2010). The large data rates (0.5–1 TB per min, or 42–84 TB per observation) and associated computational challenges necessitate data processing to be approached in multiple phases, starting with a first pass (i.e. shallow survey) as we reported in earlier papers (Bhat et al. 2023a).

The survey data collection began in 2018, and through a series of dedicated campaigns 70% of the sky was covered by mid-2021. There have been encouraging results from a partially-completed first-pass processing, including several new pulsar discoveries after a small fraction (∼5%) of the survey data analysed, and re-detections of 120 known pulsars from initial data quality checks and analysis (Bhat et al. 2023b). Among the new discoveries are a variable sub-pulse drifter (McSweeney et al. 2022), a pulsar that shows quasi-periodic nulling (Grover et al. 2024), and low-luminosity steep-spectrum objects (Swainston et al. 2021). SMART data have also been used to confirm pulsar candidates identified in image-based transient searches (Mcsweeney et al. 2025). With completion of the last SMART observation (November 2023), approximately 4 PB of data have been accrued, thus marking an important milestone, and making it the largest all-sky survey in the southern sky, and the second largest (in data volume) after the LOFAR Tied-Array All-Sky (LOTAAS) survey (Sanidas et al. 2019).

While the adoption of VCS (Tremblay et al. 2015; Morrison et al. 2023) makes longer-term data archiving tractable, the inherent complexities of calibrating and beamforming such voluminous data makes data processing rather tedious and computationally intensive, especially for routine pulsar detections and analysis. Indeed, voltage data offers enormous flexibilities through a multitude of reprocessing avenues, as newer and better algorithms and faster processing pipelines become available in the future. With an intent to better serve the wider pulsar community, and making a range of useful data products publicly accessible, we have therefore embarked on a systematic processing of SMART data sets to make a low-frequency southern-sky catalogue of pulsar detections. With the SKAO construction ramping up and a rapid progression expected in the coming years[a], it is therefore timely and important to develop such a catalogue as a living resource. The MWA is also the Australian Precursor for SKA-Low, and AA1 (Array Assembly 1, with 18 stations)[b] is expected to reach (or even surpass) the sensitivity of Phase III MWA. A comprehensive catalogue of southern pulsars detectable in the SKA-Low frequency band can thus be a valuable resource in the validation and science commissioning and verification of these stations.

As the MWA upgrade transitioned to Phase III, early prototypes were developed and commissioned for SKA-Low, providing opportunities for useful demonstrations. Over the past few years, we have taken some of the first steps in this direction, by developing pulsar capabilities for the early prototype stations for SKA-Low (i.e., EDA2 and AAVS2; Wayth et al. 2022; Macario et al. 2022), and through their commissioning and successful early science demonstrations. An initial census of pulsars and spectral analysis was reported in Lee et al. (2022), and more recently, the commissioning of the upgraded system (with a recording bandwidth of 25 MHz) enabled the first polarimetric validation as well as science application, specifically probing the magneto-ionic structure of the interstellar medium (ISM) towards the Vela pulsar (Lee et al. 2024).

The SMART survey is also motivated by several generations of past surveys; e.g., Parkes multibeam surveys (Manchester et al. 1996; Manchester et al. 2001; Keith et al. 2010). These predecessor surveys have proven very useful, both to guide and prepare the next-generation surveys, and as a reference to cross-check pulsar discoveries and detections. Re-detecting a new pulsar candidate in a past survey often yields an initial estimate of the period derivative and hence the surface magnetic field strength and characteristic age. With SKA-Low anticipated to take on a bulk of the survey load (e.g., Keane et al. 2015; Keane et al. 2025), it is imperative to have a comprehensive southern pulsar survey at low frequencies; the SMART survey will fill this gap. This motivated securing resources for longer term data archiving in addition to the MWA Data Archive, through Australia Research Data Commons (ARDC)[c], under data sets of national significance.

a. See SKAO Timeline to Science webpage.

b. SKA1 Design Baseline Description, SKA-TEL-SKO-0001075.

c. MWA SMART Survey Raw Data 2020-2021 (doi:10.25917/HNZA-1T90).

Aside from these strategic perspectives, a low-frequency pulsar catalogue is scientifically motivated on several counts. While large surveys provide subsets of such pulsar samples, the advent of large-FoV instruments, such as Low Frequency Array (LOFAR), Canadian Hydrogen Intensity Mapping Experiment (CHIME) and the MWA, also provide the ability to sample large patches of the sky instantaneously, and thus efficiently monitor or detect multiple pulsars in a single observation. Large samples of pulsars and their measurements are very useful in understanding emission properties (e.g., beam shapes and luminosity distributions), especially when low-frequency data are combined with the published measurements at high frequencies (e.g., at 1-2 GHz) using MeerKAT (e.g., Keith et al. 2024a). Measurements at low frequencies are also useful for dispersion and scattering/scintillation studies, especially for pulsars at low to moderate DMs, whereas it may be hard to discern such effects at higher frequencies ($\gtrsim$1 GHz). These are important inputs for developing improved Galactic electron density models (Cordes and Lazio 2002; Yao, Manchester and Wang 2017; Ocker, Cordes and Chatterjee 2020; Ocker and Cordes 2026) and mapping out the spatial distribution of the turbulence strength. An improved sample of low-frequency pulsar detections are also important for accurately modelling the detectable population at low frequencies (Keane et al. 2015; Xue et al. 2017; Bhat et al. 2023a), and thus inform future large surveys planned with SKA-Low.

In this sequel to the SMART survey papers (Bhat et al. 2023a; 2023b; Lee et al. 2025, referred to hereafter as Papers I, II and III), we present an updated status of survey data collection and a more complete catalogue of pulsar detections thus far, along with useful data products including the pulse profiles, time series and measurements. A census of millisecond pulsars (MSPs) was presented in Paper III. In Section 2, we present a survey update, and in Section 3 we describe various steps involved in processing data from the upgraded VCS system (known as MWAX VCS), including calibration and beamforming. The pulsar data analysis, including mitigation of radio-frequency interference (RFI) and the measurements of pulsar and ISM properties, is described in Section 4. The catalogue and enhanced data products are summarised in Section 5, some discussion and future work in Section 6, and a summary in Section 7.

2. SMART Survey: Data Collection

As described in earlier papers, through a series of four dedicated campaigns from 2018 to 2021, we advanced the SMART survey data collection to 70%, covering the sky within right ascension (RA) <16 h and >21 h and declination $\delta < +30^{\circ}$. The fourth campaign (2021A) was only partially complete before the upgrade activities commenced in earnest to build a new correlator for the MWA and implementing changes to the signal path, as part of the planned transition of the array to Phase III. The commissioning of the new MWAX correlator and VCS (Morrison et al. 2023), and associated changes to the signal path and data format, necessitated a significant revamp in the sub-system designs that constitute the high time resolu-

https://doi.org/10.1017/pasa.2026.10229

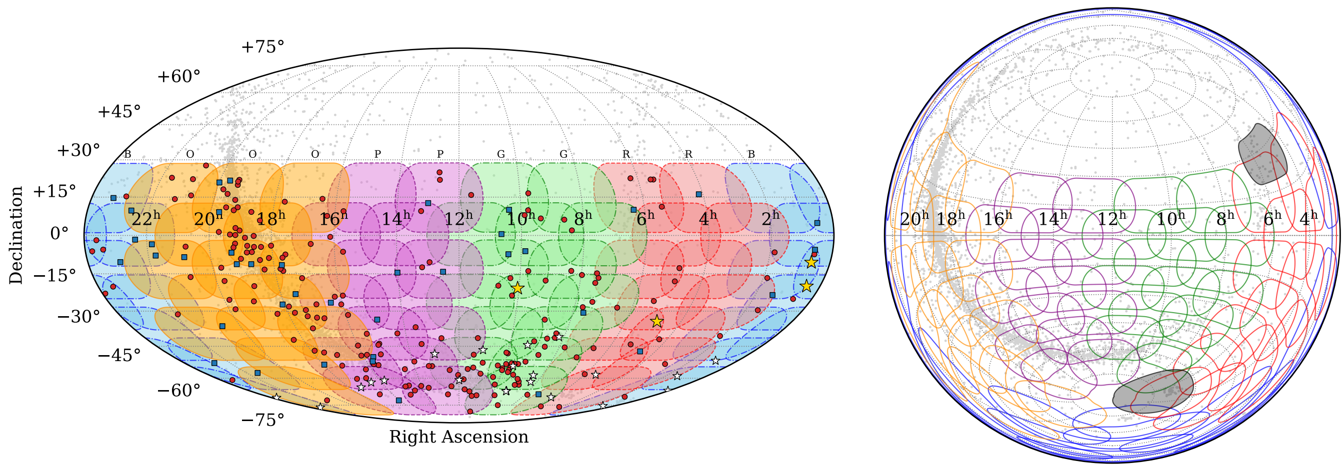

Figure 1. Sky plots in Mollweide projection (left) and Lambert azimuthal equal-area projection (right) summarising the observing strategy adopted for the SMART pulsar survey and the progress made to date with data processing. The full visible sky (i.e., declination < +30°) is covered in 71 pointings that overlap 10° in right ascension and 15° in declination. The coloured contours represent the half-power points of the main lobe of the primary beam (at 154 MHz), normalised by the maximum power in each beam. The blue, red, and green pointing sets, as well as 10 of the 14 purple ones, were observed through four dedicated observing campaigns undertaken in the 2018B, 2019B, 2020A, 2021A semesters. The remaining four purple pointings and the orange pointing set were observed in the 2023A semester. The last pointing, shown in black in the right plot, covers the South Celestial Pole (RA: 05h30m, declination −90°) and was observed in the 2023B semester. The top row of pointings are labelled by their colour to indicate the pointing set that they belong to. The red filled circles are the known non-recycled pulsar detections (205 so far), and the blue squares are the known millisecond pulsar detections (40 so far, as reported by Paper III). The yellow stars show the pulsar discoveries from the first-pass (pilot) search processing of parts of the sky (see Paper I and Paper II for further details), and the smaller white stars show the unpublished discoveries from the ongoing (second-pass) search processing. The grey dots show all known pulsars from the ATNF pulsar catalogue (v2.7.0; Manchester et al. 2005).

tion (software) backend for processing VCS recorded data, as summarised in Section 3.2.

For the legacy system, which comprised 128 tiles and performed fine channelisation (128 × 10 kHz) before recording (as 4+4 bit complex voltage samples), the associated data rate was 28 TB h^{-1}. With the higher bit depth of the new system (from a 4-bit to 8-bit sampling), the data rate is twice as large. Furthermore, recording is done following the coarse (1.28-MHz wide) channelisation, as opposed to the post-fine channelisation stage for the legacy system. This also meant adapting to new data format, and the integration of the `mwalib` package to flexibly handle data from both the legacy VCS system (until May 2021) and the new system MWAX VCS (August 2022 onward). Additionally, the installation of two new receivers as part of the ongoing Phase III integration resulted in recording additional 16 tiles (i.e. recording from all 144 tiles by default, in place of previously 128), and consequently, an increased data rate of 64 TB h^{-1}, which is a significant step up from the earlier 28 TB h^{-1}. The longer baselines of additional tiles, in principle, may offer the benefits of improved localisation for new pulsar discoveries, and therefore the final campaign employed recording from all 144 tiles. A summary of these SMART campaigns is given in Table 1, along with details like the amount of data collected and the number of pulsars detected thus far.

The final observing campaign was carried out in the 2023A observing semester, which covered the incomplete pointings from the 2021A (fourth) campaign (i.e. purple pointings) as well as the full sky in the 16 < RA < 21 h and $\delta < +30^{\circ}$ (i.e. orange pointings) through 15 + 4 = 19 VCS pointings, the details of which are summarised in Table 1. Additionally, a dedicated SMART observation was made towards the South Celesial Pole (SCP), as otherwise this part of the sky would end up with only partial low-sensitivity coverage. As can be seen from the survey sky map in Figure 1, there is ∼20% overlap in the sky coverage with earlier campaigns (blue and purple pointings), and that is to do with the nature of our survey design, where every single patch of the sky is covered in at least two pointings at a gain above the half power (primary) beam level. The total data collected from the final campaign is 1621 TB from a total of 19 pointings, thereby bringing the net data collection from SMART to ∼3.9 PB (from a total of 71 pointings). Further details of the SMART pointings including the coordinates of the pointing centres and observation IDs (Obs IDs) for VCS and calibrator observations are listed in Table 2. These data sets effectively represent a digital version of the entire sky south of $+30^{\circ}$, and serves as a unique permanent record of the electromagnetic state of the sky. The native resolutions (for the legacy VCS data) are 100 µs, 10 kHz in time and frequency, respectively; however, these can be reprocessed for higher time resolution (down to ∼ 1 µs) using a synthesis filter (McSweeney et al. 2020). As such the SMART datasets hold an enormous legacy value, and recording as voltages (instead of beamformed data) makes their long-term archiving tractable.[d]

d. With a data rate of 138 GB per beam (for 4800 s), beamforming will result in a significant data explosion; e.g., 670 TB from a single observation when tessellated into 5000 beams across the ∼610 deg^2 FoV.

https://doi.org/10.1017/pasa.2026.10229

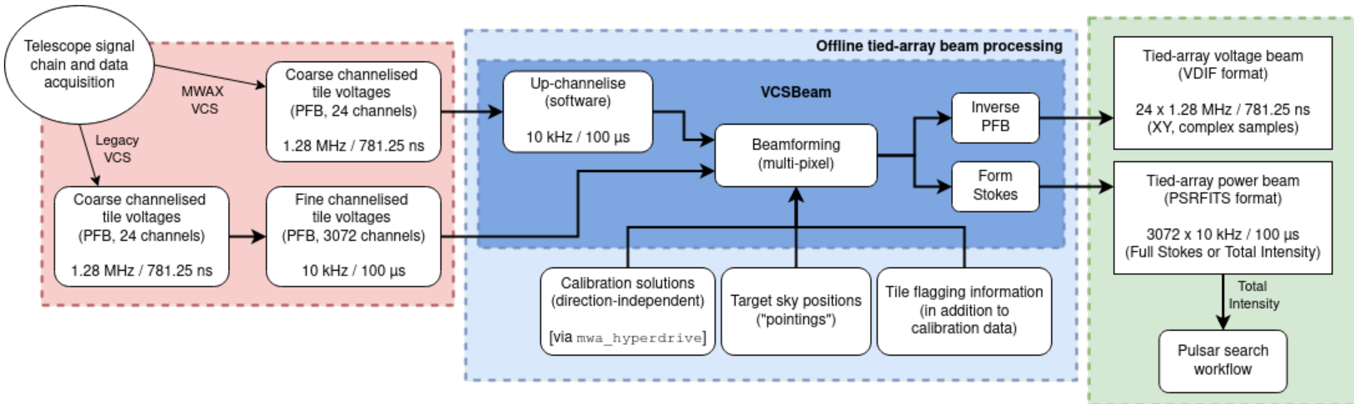

Figure 2. The signal path and processing workflow that makes the subsystem for the high-time resolution science observations with the MWA. With the legacy system (retired in August 2021), voltage data are recorded after two stages of polyphase filterbank (PFB) channelisation, resulting in 3072 × 10-kHz voltage time series at 100-µs resolutions, which can be then beamformed on targets of interest after the calibration procedures. The beamformed data are written out as detected full Stokes, or summed polarisation (for the SMART survey project) at the native 100-µs/10-kHz resolutions, or can be reprocessed using an inverse synthesis filter to produce a higher resolution (≈0.78 µs) time series (e.g., for MSP observations). With the new system (MWAX VCS; starting October 2021), voltage data are recorded directly after the coarse channelisation (24 × 1.28-MHz wide channels), which can be then processed (offline) in different ways. In the 'SMART' mode, data in an identical format to the legacy system are generated after applying a fine PFB (in software), to result in 100-µs/10-kHz resolutions. For other science applications that require higher time resolution (e.g., MSPs) or visibility data (e.g., FRBs) the same data can be processed using suitable alternatives to the VCSBEAM suite of software tools. See text for further details.

Table 1. Summary of the SMART survey observing campaigns.

Observing semester	Dates of observation	No. of VCS pointings	Pointing labels††	RA range (hr)	Data collected (TB)	Re-detected pulsars†	New pulsars‡
2018B	September – December 2018	13	B01–B13	22–3	546	24 (0)	9
2019B	September – December 2019	13	R01–R13	2–7	546	29 (1)	2
2020A	January – March 2020	15	G01–G15	6–12	630	62 (6)	10
2020B	March – May 2021	10	P01–P10	12–16	420	34 (0)	1
2023A	April – August 2023	4	P11–P14	12–16	256	25 (0)	3
2023A	April – August 2023	15	O01–O15	16–21	1280	80 (2)	
2023B	November 2023	1	SCP	5–6	85	1 (1)	

† The number in parentheses are common re-detections with the previous semesters.
‡ New pulsars discovered thus far in the ongoing processing; unpublished ones will be reported in a future paper in the SMART series.
†† See Table 2 and Figure 1 for details; the label ID corresponds to Blue, Red, Green, Purple and Orange pointings as shown in Figure 1, and SCP denotes the pointing towards the South Celestial Pole.

The successful completion of data collection marks a significant milestone for the SMART survey project. As described in earlier papers, we first performed a *shallow* survey of a small fraction (∼5%) of the sky, reaching approximately one-third of the full-search sensitivity. This effectively served as a proof-of-concept. We emphasize that due to the drift-scan nature of SMART observations, the *effective on-source time* will vary depending on the pointing and the offset relative to the beam centre, as discussed in Paper I (cf. Section 2.5, Figures 3 and 4). The ongoing deep-pass processing involves processing the full 4800-s observations; this commenced in September 2024, resulting in the discovery of 23 new pulsars after processing ∼10% of data. Follow-ups of these are in progress and will be reported in a future paper, where we will also describe the extended search pipeline and processing strategies.

3. Processing MWAX VCS Data

The SMART project also strongly motivated the development and commissioning of the software subsystem VCSBEAM that was pivotal for survey completion. VCSBEAM was developed as a flexible software that can process data from both legacy and the new (MWAX) VCS systems. Furthermore, developments on the calibration side have enabled us to undertake a systematic processing of all calibration observations in a uniform manner. As these new software and processing steps will become the standard for the routine processing of VCS data from here on, we will summarise the related procedures here, as a useful reference. This involves obtaining calibration solutions using dedicated observations of calibrators (recorded in the visibility mode), and generating data in identical format to the legacy VCS system (i.e. 100-µs/10-kHz resolutions). An overview of the related signal path and processing workflow is presented in Figure 2.

3.1 Phase and amplitude calibration

For each of the SMART observations, there are a handful of standard calibration observations taken before and after the nominal voltage (VCS) recording. These are required in or-

https://doi.org/10.1017/pasa.2026.10229

der to derive the relative complex amplitudes and phases of each MWA tile (as a function of frequency channel), which are a critical part of the beamforming process. This collection of tile-based amplitudes and phases across the observing bandwidth are the 'calibration solution.' We transfer these calibration solutions from the standard calibrator field to the SMART observation field – the MWA is generally phase-stable on reasonably long time scales, and our experience has been that the use of a single calibration solution works well over ∼4800-s observing durations of SMART pointings.

To extract the calibration solution, we used the purpose-built BIRLI[e] and MWA_HYPERDRIVE[f] packages on the dedicated calibration observation. First, BIRLI is used to flag known misbehaving tiles (based on metadata collected by the observatory during observing sessions), apply passband, digital gain and geometric corrections, perform basic radio frequency interference (RFI) mitigation, and average the visibilities to 2-s/40-kHz resolution. These pre-processed visibilities are then passed to MWA_HYPERDRIVE, along with nominal sky and primary beam models, which attempts to solve for the amplitude and phase of each tile at each frequency channel and incorporates ionospheric refractive source shifting effects (Jordan et al. 2025), i.e., bulk source position offset correction across the field-of-view. This amounts to a direction-independent calibration procedure that is equivalent to an iterative application of the classic *antsol* approach (e.g., Bhatnagar and Nityananda 2001; Mitchell et al. 2008). The calibration solutions obtained in this manner are collated at a central repository and can be used to expedite future re-processing. In general, there are two or more dedicated calibrator observations for each SMART observation, and the one that maximises the detection sensitivity of known bright pulsars in the field is adopted as the preferred calibration solution for a given observation.

3.2 Tied-array beamforming with VCSBeam

The algorithm used for the beamforming operation in VCSBEAM[g] is identical to that described by Ord et al. (2019), with the addition of the multi-pixel functionality (Swainston, Bhat et al. 2022) and the ability to invert the polyphase filterbank (PFB) to produce coarse-channelised VDIF (VLBI data interchange format) data (McSweeney et al. 2020). To summarise, the basic beamforming operation involves:

1. Applying a predetermined calibration solution to complex-valued voltages, to account for differences between the responses and signal paths of each MWA tile and polarisation (Section 3.1);
2. Adding a term to the phases of the voltages to account for the geometric delay of a signal coming from the target look-direction;
3. Summing the voltages from each tile/polarisation together; and
4. (Optionally) converting the dual polarisation beamformed voltages to Stokes parameters.

e. https://github.com/MWATelescope/Birli
f. https://github.com/MWATelescope/mwa_hyperdrive
g. https://github.com/CIRA-Pulsars-and-Transients-Group/vcsbeam

The advent of the MWAX backend removed the fine-channelisation (i.e. the second PFB stage) step that was previously performed by dedicated field programmable gate array (FPGA) boards on site before the signal was passed to either the correlator or the VCS backend (cf. Tremblay et al. 2015). Consequently, MWAX voltage data are written to disk as coarse-channelised, Nyquist-sampled voltages (1.28 MHz). We therefore re-implemented the PFB in software and added it as a new module to VCSBEAM (see Figure 2). In doing this, backwards compatibility is maintained: i.e. the PFB is only applied if the VCS observation is of the MWAX VCS type. In the case of legacy VCS data, the sampled voltage time series is already fine channelised (i.e. 10-kHz/100-μs resolutions).

The PFB implementation in VCSBEAM can be run in two additional modes that were not available in the FPGA implementations. Firstly, the output voltages can be either typecast into 4-bit complex integers (as in the FPGA implementation), or retain the full 64-bit floating point ('double') precision used during the calculation. In terms of computing resources (runtime, memory), there is no disadvantage to using the latter, since the voltages stay in memory, and are promoted to 64-bit floats during beamforming in any case. We have found, however, that the retention of the full precision makes negligible difference to the signal-to-noise ratio (S/N) of the final beamformed products. Secondly, the asymmetric rounding scheme of the FPGA PFB, described in the appendix of McSweeney et al. (2020), has been replaced with symmetric rounding; however, the original asymmetric scheme is still available as an option. To keep the data products from SMART as homogeneous as possible, we have included a specialised 'SMART' option which reproduces the FPGA implementation of the PFB exactly. The deleterious effects of demoting to 4-bit integers and using an asymmetric rounding scheme are found to be marginal.

Some aspects of VCSBEAM have been improved to make better use of the available compute resources, especially when executed on a supercomputing infrastructure. For instance, VCSBEAM makes use of Message-Passing Interface (MPI) to handle the embarrassingly parallel processing of multiple coarse channels, as well as gathering the channels together to write out a single PSRFITS file. Multiple seconds of data, corresponding to several files for each coarse channel, are read in parallel using CPU threads and buffered into computer memory. The approach leverages the high data-transfer bandwidth of a distributed filesystem while limiting the impact of latency and resource contention. The core beamforming GPU kernel itself has also evolved to employ modern GPU programming techniques that make more efficient use of modern GPUs. Benchmarked on an AMD MI250X GPU of Pawsey's Setonix supercomputer, the execution time of the compute kernel has improved by a factor of 8 compared to the original GPU implementation on the same hardware. Further, VCSBEAM can be compiled for both NVIDIA and AMD GPUs, allowing the software to run on the majority of modern supercomputing infrastructure.

https://doi.org/10.1017/pasa.2026.10229

4. Pulsar Data Analysis

Beamformed data from VCSBEAM can be written out either in PSRFITS format (Hotan, van Straten and Manchester 2004) at 100 μs/10 kHz native resolutions (i.e. identical to the legacy VCS system) or as voltage time series in VDIF format[h], in which case the data are stored as 24×1.28 MHz coarse channels. Our intent is to make these publicly available along with a number of data products and measurements that are science-ready. The choice of these common data formats means the data can be readily processed using standard packages such as PRESTO, DSPSR and PSRCHIVE. While DSPSR can operate on both output formats, PRESTO can ingest only the PSRFITS output. Our detections are summarised in Table 3, where we also list the integration times ($T_{\rm obs}$).

In the vast majority of cases, $T_{\rm obs}$ is in the 30–80 min range; this variation is mainly due to different lengths of data that were downloaded or available at the time of processing. In the cases where the pulsar was visible for only a fraction of the duration (e.g., due to effective on-source time less than 80 min), we have chosen to analyse just the data segment where the zenith-normalised primary beam power towards the pulsar was greater than 20%. As a result, for many of the detected pulsars, it is possible to obtain improved detections through longer targetted integrations, where applicable. Below, we outline the main steps in the analysis of beamformed data to generate various data products of interest, such as the pulse profiles and folded archives, as well as various measurements relating to the pulsar emission and ISM propagation effects.

4.1 Dedispersion and folding

For the standard data analysis of non-recycled pulsars presented in this paper, we incoherently dedisperse and fold PSRFITS files using DSPSR at the native frequency channel resolution (10 kHz) with 10-second subintegrations and 256 phase bins. The folded data are stored in the PSRFITS archive format, enabling flexible data analysis with PSRCHIVE. In contrast with the non-recycled pulsar detections, the MSP detections in Paper III were phase-coherently dedispersed and folded with up to 1024 phase bins. However, the flux densities, DMs, and RMs have been measured using the same methods for both the non-recycled pulsars and the MSPs. These methods will be briefly summarised here for completeness.

4.2 RFI mitigation

The exceptionally radio-quiet nature of the Observatory site (in comparison to most other observatories) and our preferential strategy for SMART survey observations to be during nightly hours make the mitigation of radio-frequency interference (RFI) non-essential for the majority of routine pulsar data processing. Indeed, sensitive pulsar searches will benefit from a careful assessment of the periodic RFI environment (and devising suitable steps to mitigate it), and this is part of the SMART processing plans under active development. Typically, much of the SMART data are remarkably clear of RFI, and even extreme cases (due to either impulsive or narrowband type RFI) are limited to a small fraction ($\lesssim$10%) of the data. Importantly, having access to full-resolution data allows PRESTO tools (such as `rfifind`) or PSRCHIVE tools (such as `paz`, `pazi`, or `psrzap`) to be effectively used to excise any RFI present in our data. Oftentimes, this tends to be science-dependent, and so we prefer to retain that flexibility for users. However, for folded data products, we have opted to perform automated RFI mitigation using CLFD (Morello et al. 2019). In our testing, this is sufficient to remove the majority of obvious RFI.

4.3 Improved dispersion measures

The ~20% fractional bandwidth of SMART data (30.72 MHz centred at 154.24 MHz) is quite comparable to previous pulsar surveys in the southern skies – for instance, the Parkes multibeam surveys employed 288 and 380 MHz of bandwidth for the legacy and HTRU surveys, respectively (Manchester et al. 2001; Keith et al. 2010). The inverse-frequency-square law dependence of the dispersion delay ($t_{\rm dm} \propto \nu^{-2}$, where ν is radio frequency) still means a much longer frequency lever arm in the SMART frequency band, which allows us to make precise measurements of DMs, even from a single detection with a modest S/N. Indeed, higher precisions (down to $\sim 10^{-6}$ cm^{-3} pc) can be achieved when observations are made in a distributed channel set up, and with phase-coherent dedispersion techniques, as we have demonstrated in observations of MSPs (Kaur et al. 2019; Kaur et al. 2022). For non-recycled pulsars in the SMART data, we typically limit our processing to incoherent dedispersion within the 30.72 MHz contiguous bandwidth.

The improved DMs obtainable from the SMART data are especially important for two main reasons. Firstly, in cases where the catalogued DMs are inaccurate or imprecise, these low-frequency measurements may provide better measurements. Secondly, in the case of frequency-dependent DMs (cf. Cordes, Shannon and Stinebring 2016) that arise from multipath propagation effects, DM measurements at low frequencies may differ in measurable ways to those from higher radio frequency observations (e.g. Kaur et al. 2022). Aside from this subtlety, it is conceivable that profile evolution in frequency can potentially result in some systematic bias between the measured DMs. With observations using wide-band instrumentation becoming a common practice, this seems especially relevant (e.g. Hassall et al. 2012). We therefore measure and tabulate DM measurements from our SMART detections.

As with our earlier partial census published in Paper II, the vast majority of our pulsar detections are in the signal-to-noise ratio (S/N) range ~10–100 in 30–80 min observations over the full SMART frequency band. For the purpose of DM determination, we make use of the `pdmp` routine from PSRCHIVE to perform a fine search in period and DM. We perform the search with 10-second subintegrations and 320 kHz subbands with a DM step size[i] of 0.005 cm^{-3} pc (for non-recycled pulsars) or 0.001 cm^{-3} pc (for MSPs). When a DM correction of 2σ or

h. https://vlbi.org/vlbi-standards/vdif/

i. Due to the nature of the `pdmp` algorithm, the reported best DM may not be an integer multiple of the step size.

https://doi.org/10.1017/pasa.2026.10229

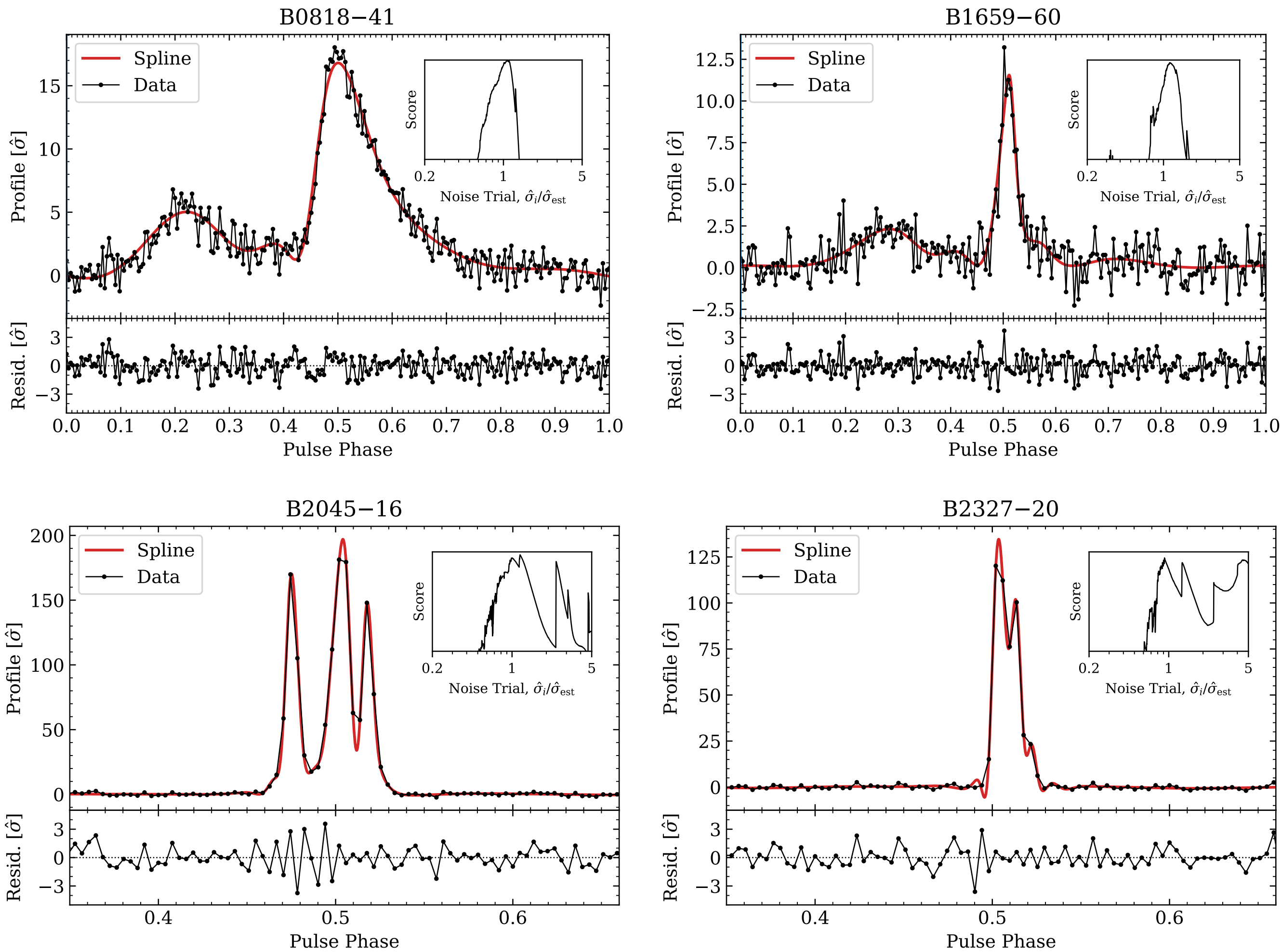

Figure 3. Example spline fits to the integrated pulse profiles of PSRs B0818–41 (top left), B1659–60 (top right), B2045–16 (bottom left), and B2327–20 (bottom right). The top panel of each subfigure shows the measured profile (black connected dots) and the spline fit (red lines), whilst the bottom panel shows the fit residuals. The insets show the heuristic 'whiteness' score of the residuals for a range of noise trials, $\hat{\sigma}_i$, which determine the smoothing factor $s = N_b\,\hat{\sigma}_i^2$ (see Section 4.4 for details). The spline fit to B2327–20 exhibits oscillations at the leading and trailing edges due to the sharp transitions.

greater is measured, we correct the residual dispersion delays using the `pam` routine. A drift in period is seldom seen in our data as we make use of most up-to-date pulsar ephemerides available, either from MeerTime[j] (Keith et al. 2024a; Keith et al. 2024b) or from the ATNF Pulsar Catalogue (Manchester et al. 2005). In the rare cases where a period correction is needed, we use the S/N-optimised value reported by `pdmp`.

4.4 Integrated pulse profiles and pulse widths

For each pulsar detection, we average the subintegrations and frequency channels to produce an integrated pulse profile. The detected sample of pulsars includes a diverse range of profile shapes, including a number of profiles with broadening due to multipath propagation in the ISM. The complexity of the profiles, along with the range of S/N ratios, makes it challenging to reliably measure pulse widths without component fitting, which is difficult to reliably automate. Nevertheless, measurements of pulse widths are important for studies of the intrinsic frequency-dependence of pulsar emission and scattering in the ISM.

Considering that we primarily want to model the profiles to estimate the pulse widths and onpulse phase regions, we have chosen to model each profile by fitting a smoothing spline; i.e., a smooth curve constructed from multiple polynomial segments that are joined seamlessly at boundary points called 'knots'. We use the `splrep` function[k] from SCIPY to find the number and location of the knots, and the coefficients of the basis polynomials. This approach enables the straight-forward computation of profile derivatives, which can be used to estimate the onpulse/offpulse. We fit splines of degree 5 (so that the second derivative is a cubic spline) with periodic boundary conditions at the edges of the pulse profile.

j. https://pulsars.org.au/

k. `splrep` is a Python wrapper for a subroutine of the same name from the Fortran library FITPACK (Dierckx 1975). It is documented here: https://docs.scipy.org/doc/scipy/reference/generated/scipy.interpolate.splrep.html

https://doi.org/10.1017/pasa.2026.10229

The splrep fitting algorithm takes a smoothing condition, s, which determines the 'rigidity' of the spline; it should be chosen such that the noise in the profile is removed whilst retaining as much pulse structure as possible (i.e. to avoid over- or under-fitting). In general, a good choice of smoothing condition is $s \sim N_b \hat{\sigma}^2$, where N_b is the number of phase bins and $\hat{\sigma}$ is the standard deviation of the noise in the profile. To find the best-fit spline, we performed a log-spaced grid search in the range $\hat{\sigma} \in [0.2\hat{\sigma}_{est}, 5\hat{\sigma}_{est}]$, where $\hat{\sigma}_{est}$ is an initial estimate of $\hat{\sigma}$. We determined $\hat{\sigma}_{est}$ by finding the phase window of width $N_b/8$ bins with the minimum integrated flux density, and measuring the standard deviation of the sample values in that window. For each trial i, we fit a spline with $s_i = N_b \hat{\sigma}_i^2$ and performed the following tests:

- a Ljung-Box test, where the null hypothesis is that all of the autocorrelations of the residuals up to a lag of 20 samples are jointly zero; and
- a Wald-Wolfowitz runs test, where the null hypothesis is that the sequence of signs of the residuals above or below the mean is random.

We then multiplied the p-values of the two tests to determine a heuristic score for the 'whiteness' of the residuals[1]. The spline with the maximum score was selected as the best fit. Our testing indicates that this method yields reasonable fits for a wide range of profile shapes. In Figure 3 we show the best-fit smoothing splines for four pulsars with a variety of profile features. PSRs B0818–41 and B1659–60 have broad features that are well modelled by a more rigid spline, whereas PSRs B2045–16 and B2327–20 have sharper features (relative to the bin width). The best-fit spline for B2327–20 exhibits 'Runge's phenomenon', where sharp transitions induce oscillations in high-degree polynomials (in this case degree 5) fitted to equispaced samples. Increasing the number of phase bins would likely improve the fits; however, we have opted to uniformly process with 256 phase bins for this work. On the other hand, for pulsars with structure at a similar timescale to the bin width, the smoothing spline interpolates peaks and troughs in the profile (see B2045–16 and B2327–20 in Figure 3). In some cases, this may improve the estimate of the peak amplitude. However, for the peak flux densities listed in Table 3 and Figure 4, we have used the peak of the data rather than the spline, as we are not confident that the spline fits consistently give more accurate estimates of the peak amplitude.

To estimate the onpulse regions, we identified the maxima of the spline which exceed $3\hat{\sigma}$, and then the corresponding minima of the spline which flank these maxima. The intervals between the flanking minima were considered part of the onpulse. If none of the samples between two of the initially identified onpulse regions fell below $1\hat{\sigma}$, the two regions were considered to be part of the same onpulse region. Lastly, if multiple pulse components were identified nearby in phase (e.g. PSRs B0148–06 and B0957–47 in Figure 4), they were considered part of the same onpulse region – i.e. interpulses were treated separately where they could be identified, but otherwise the components were considered part of the same onpulse region.

Spline fitting enables estimation of the profile widths by solving for the roots at a given amplitude. As such, for all detections with peak amplitudes greater than $2\hat{\sigma}$ and $10\hat{\sigma}$, respectively, we measured W_{50} and W_{10} (i.e. the pulse width at 50% and 10% of the peak amplitude). For consistency, the peak amplitudes used for estimating the 50% and 10% amplitudes were measured from the spline fits. Each profile fit was visually inspected to verify that the pulse width measurements are reliable.

4.5 Mean flux densities

The system sensitivity was simulated following the method described by Meyers et al. (2017) and Paper III, which involves simulating the tied-array beam over the whole sky. To account for the direction and frequency dependence of the beam, the sensitivity was estimated from the average of four uniformly spaced time and frequency steps, for a total of 16 simulations per observation. It should be noted that this does not fully correct the bias introduced by beam fading (i.e. the change in on-source power over time), so we have limited our analysis to periods when the target is above 20% beam power at 154 MHz. The simulations are used to estimate the noise expected in each phase bin, $\hat{\sigma}_{sim}$. The mean flux density S_{mean} was then calculated as follows:

$$S_{mean} = \frac{1}{N_b} \frac{\hat{\sigma}_{sim}}{\hat{\sigma}_{data}} \sum_{i=1}^{N_b} (p_i - \bar{p}_{off}), \tag{1}$$

where N_b is the number of phase bins, $\hat{\sigma}_{data}$ is the standard deviation of the noise in the profile estimated from the spline-fit residuals (see Section 4.4), p_i is the uncalibrated flux density of the ith phase bin, and $\bar{p}_{off}$ is an estimate of the profile baseline calculated from the mean of the offpulse samples. By estimating $\hat{\sigma}_{data}$ from the spline-fit residuals, we are able to estimate the noise level reliably, even for pulsars with small or non-existent offpulse regions (e.g. due to scatter broadening). For the pulsars with no offpulse samples (e.g. scattered pulsars such as B0531+21, B0833–45, and B1844–04), $\bar{p}_{off}$ was measured from a short phase window that minimised the integrated flux density. For each mean flux density, we assign a statistical uncertainty $\hat{\sigma}_{sim}/\sqrt{N_b}$ and a systematic uncertainty of 30% for sources away from the Galactic plane ($|b| > 10^\circ$) and 40% for sources near or on the Galactic plane (for a discussion on the sources of systematic uncertainty, see Section 3.2.1 of Paper III). For the peak flux density, the statistical uncertainty is simply $\hat{\sigma}_{sim}$. The statistical and systematic uncertainties were summed in quadrature to calculate the total uncertainty.

4.6 Faraday rotation measures

For each detection, we measured the profile-averaged RM following the method described in Paper III. To summarise, we measured the Faraday dispersion function (FDF) for all of the onpulse phase bins, then added the amplitudes of the

1. Since the two tests are not independent, the product of the p-values is not a valid test of the joint null hypothesis.

https://doi.org/10.1017/pasa.2026.10229

FDFs together to make a profile-averaged FDF. The RM was determined as the Faraday depth for which the amplitude of the FDF peaked. This procedure was bootstrapped by adding white noise to the data to create a sample of RM point estimates. For low-S/N cases with multiple peaks in the bootstrap distribution due to noise, we discarded samples outside of the RM peak, which was typically easy to identify by manually inspecting a histogram of the samples. We then measured the mean and standard deviation of the bootstrap samples to estimate the RM and the 1σ statistical uncertainty.

For pulsars with catalogued RMs below 300 rad m^{-2}, we performed the search in the range $[-300, 300]$ rad m^{-2} with 80 kHz subbands. For pulsars with unknown RMs or catalogued RMs above 300 rad m^{-2}, we performed the search in the range $[-600, 600]$ rad m^{-2} with 40 kHz subbands. The chosen frequency resolutions ensure that sensitivity is maintained within the search range (Brentjens and de Bruyn 2005). All searches were done with a Faraday depth resolution of 0.2 rad m^{-2}, which oversamples the FDF by a factor of $\sim$12.5.

The estimated ionospheric contribution $\mathrm{RM_{iono}}$ was subtracted from the observed value $\mathrm{RM_{obs}}$ to estimate the RM due to the ISM, i.e. $\mathrm{RM_{ISM}} = \mathrm{RM_{obs}} - \mathrm{RM_{iono}}$. Details on the estimation of $\mathrm{RM_{iono}}$ are discussed in Paper III. In short, we use SPINIFEX (Mevius, Thomson and Dijkema 2025) for spatial and temporal interpolation of the total electron content (TEC) using a single-layer ionospheric model with global ionospheric measurements (from the JPL). The uncertainties in $\mathrm{RM_{iono}}$ calculated by SPINIFEX are doubled to better reflect the accuracy observed previously in pulsar observations at the telescope site (Lee et al. 2024).

5. Catalogue and Enhanced Data Products

Figure 4 and Table 3 provide a summary of our detections and enhanced data products derived from them. As mentioned earlier, the focus in this paper is 205 known non-recycled pulsars detected in SMART data from the processing so far (two of these being earlier SMART discoveries from the shallow survey). Similar information for 40 MSPs have been presented in Paper III, while new pulsars discovered in the search processing so far will be covered in a forthcoming publication. In total, we have detected 245 known pulsars thus far in the SMART band, and counting 23 additional pulsar discoveries from the SMART survey that have not been included in the census (see Section 2, Figure 1), we have 268 pulsars detected in the SMART data. In effect, the combination of Paper III and Paper IV (this work), and the forthcoming one (on new discoveries), represent the first data release, or SMART DR1. While the processing strategies are slightly different for the two samples in Papers III and IV (e.g. coherent vs incoherent dedispersion), we maintain uniformity in the data sets and measurements presented. These are intended to be a living resource as we add more when new detections flow in from our processing.

There have been several studies in the recent past reporting low-frequency pulsar detections using northern facilities. Pilia et al. (2016) measured the pulse widths for a sample of 100 pulsars in the LOFAR low (15–62 MHz) and high (120–167 MHz) bands, and more recently, Kumar et al. (2025) report a census of 100 pulsars in the LWA 20–88 MHz band. Low-frequency flux density measurements were reported by Bilous et al. (2016) for 158 pulsars using LOFAR high band observations (110–188 MHz), and subsequently (Bilous et al. 2020) extended this work to the lower band (40–78 MHz) for a subsample of pulsars. Kumar et al. (2025) also report flux density measurements for their detections down to 20 MHz. More recently, Kumar, Sokolowski and Wayth (2026) extended the work of Lee et al. (2022), reporting pulse profiles and flux densities for 120 pulsars using the EDA2, an SKA-Low prototyping station comprising 256 MWA dipoles ($\sim$10% of the Phase II MWA sensitivity for the same bandwidth). Additionally, Malofeev, Malov and Shchegoleva (2000) report detections and flux densities for 235 pulsars at 102.5 MHz with the Large Phased Array (LPA or BSA). More recently, Tyul'bashev, Kitaeva and Tyul'basheva (2022) report the detections of 161 northern pulsars at 111 MHz in the Pushchino mulibeam pulsar search; however, they do not provide any profiles or flux density measurements.

The major distinction is, with the exception of EDA2 measurements, most of the previous measurements are for northern pulsars (LOFAR, LWA, or LPA/BSA) and have a wider frequency coverage (extending down to frequencies below 100 MHz); whereas, our SMART pulsar sample is in the 140–170 MHz band. Detailed comparisons of overlapping sub-samples may still be useful but are outside the scope of current work. However, we include some brief commentaries where applicable, and as such some of these aspects will be the subject of forthcoming papers. Together, these low-frequency samples and measurements will serve as a valuable reference for SKA-Low science verification, and more generally for exploring the frequency dependence of pulsar emission properties and/or flux-density spectra at lower frequencies.

Furthermore, the overlap design of SMART survey (see Figure 1) means a given sky patch is typically sampled 2–3 times, and hence multiple detections are possible. In principle, these can be co-added to produce better detections; however, the data-intensive nature of VCS processing (a typical SMART observation is $\sim$38–84 TB) makes the full observation processing both tedious and time-consuming for our petabyte-scale data volumes. We therefore intend to periodically update our database and detections, as processing moves forward, and as and when new pulsars are detected or better detections are obtained on previously detected ones.

5.1 *Pulse profiles*

The integrated pulse profiles for the best detections (by S/N) of the 205 pulsars re-detected in the SMART data are presented in Figure 4. Since the previous census reported in Bhat et al. (2023b), many of the pulsar detections have been reprocessed with longer integration times and additional RFI mitigation, and hence are present here with a higher S/N. Figure 5 shows the W_{10}–W_{50} distribution for the non-recycled pulsars for which both width measurements could be made.

https://doi.org/10.1017/pasa.2026.10229

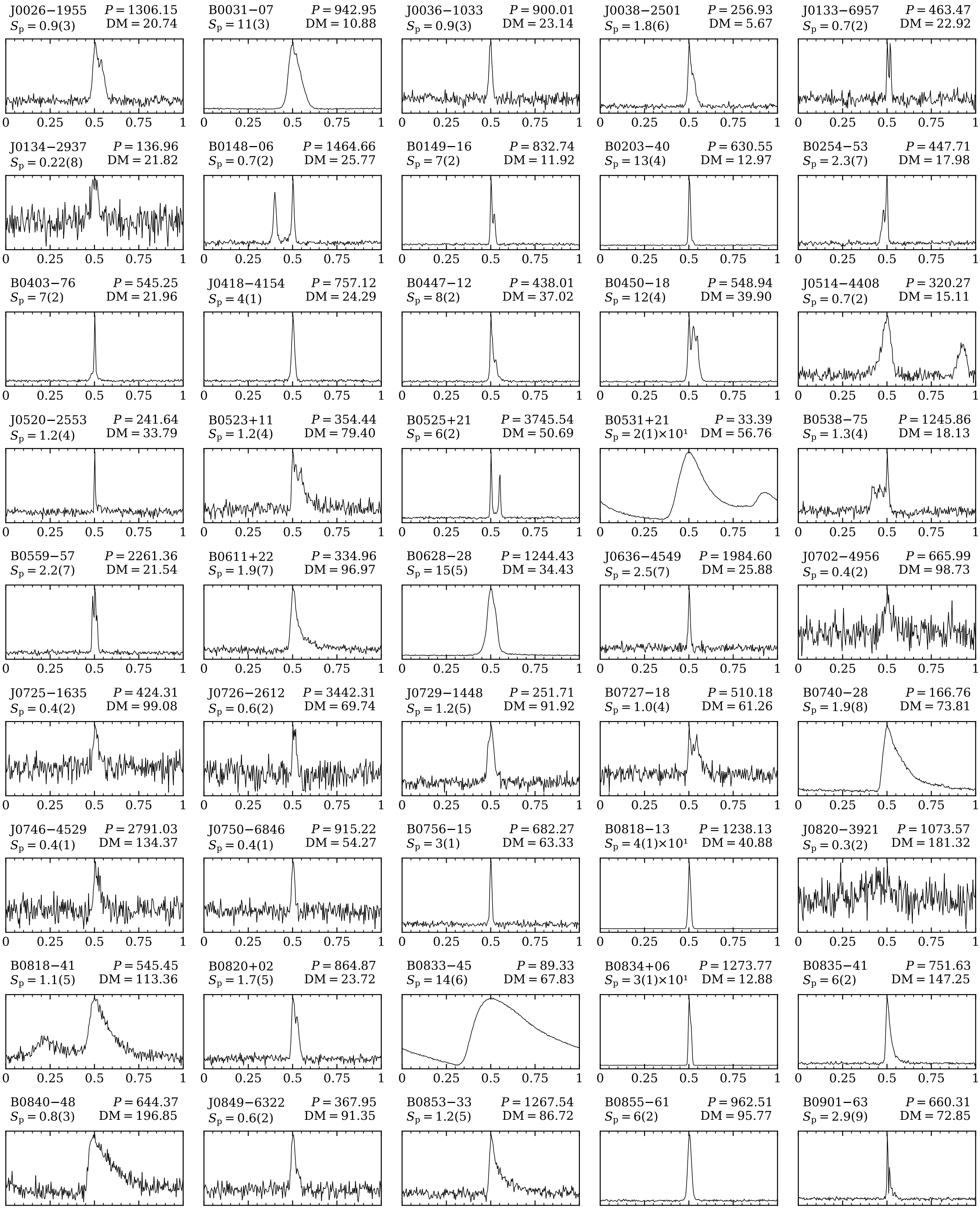

Figure 4. Integrated pulse profiles for the best detection of each of the 205 non-recycled pulsars in SMART observations. For each pulsar, we list the B-name (or if unavailable, we use the J-name instead), the spin period in ms, the DM in $\mathrm{cm^{-3}\,pc}$, and the peak flux density S_p in Jy (the uncertainty in the last digit is listed in parenthesis, rounded to 1 significant figure).

https://doi.org/10.1017/pasa.2026.10229

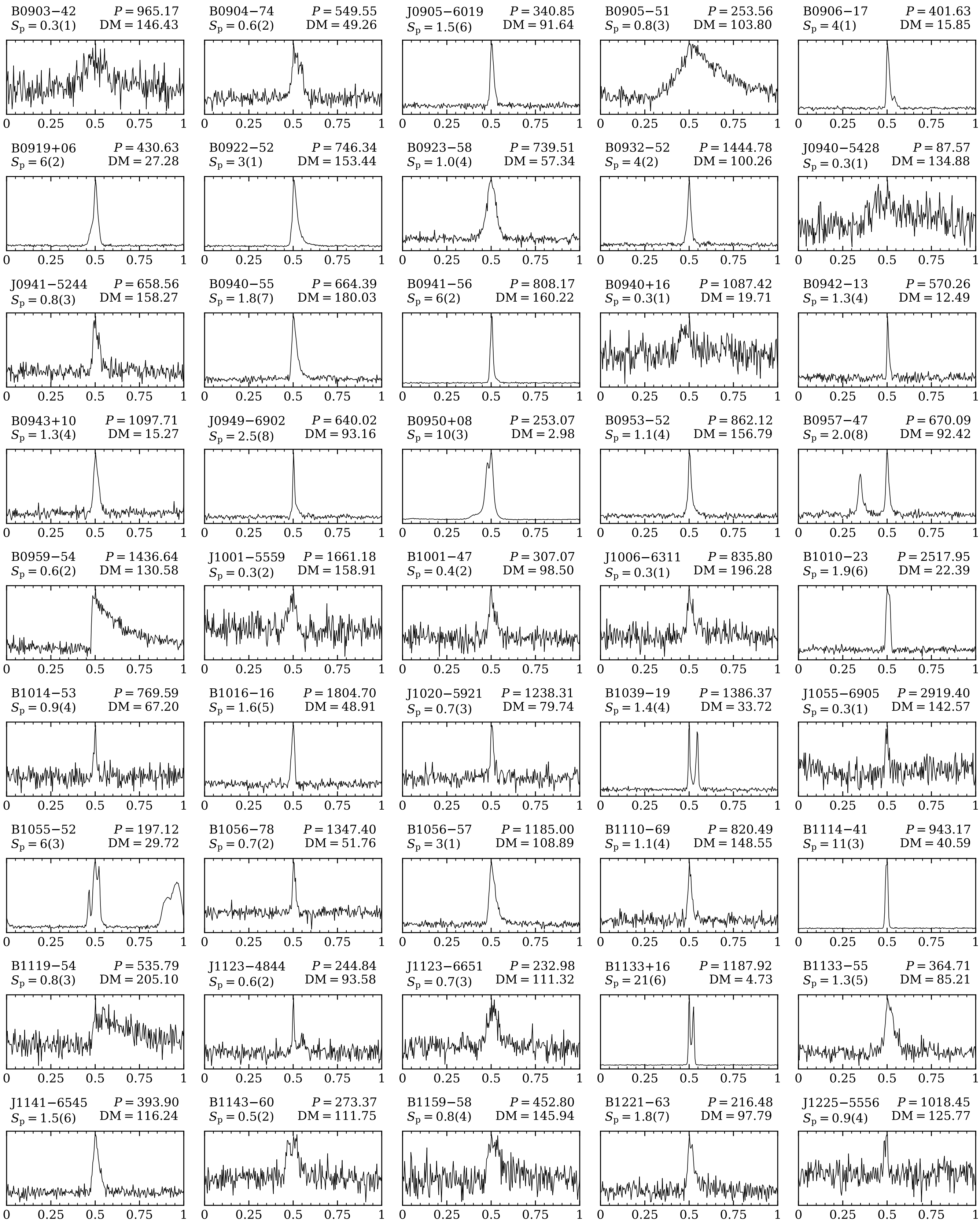

Figure 4. Continued.

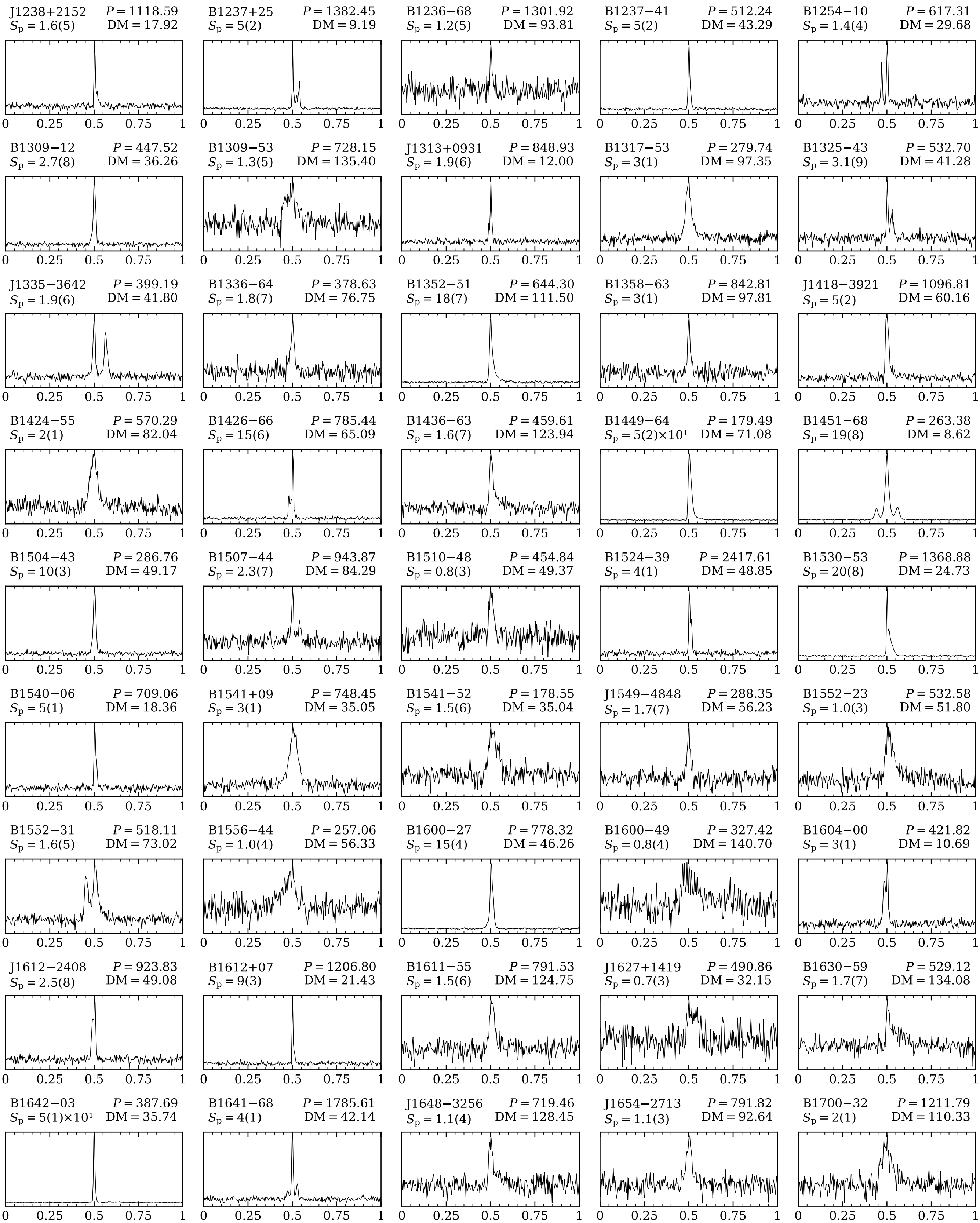

Figure 4. Continued.

https://doi.org/10.1017/pasa.2026.10229

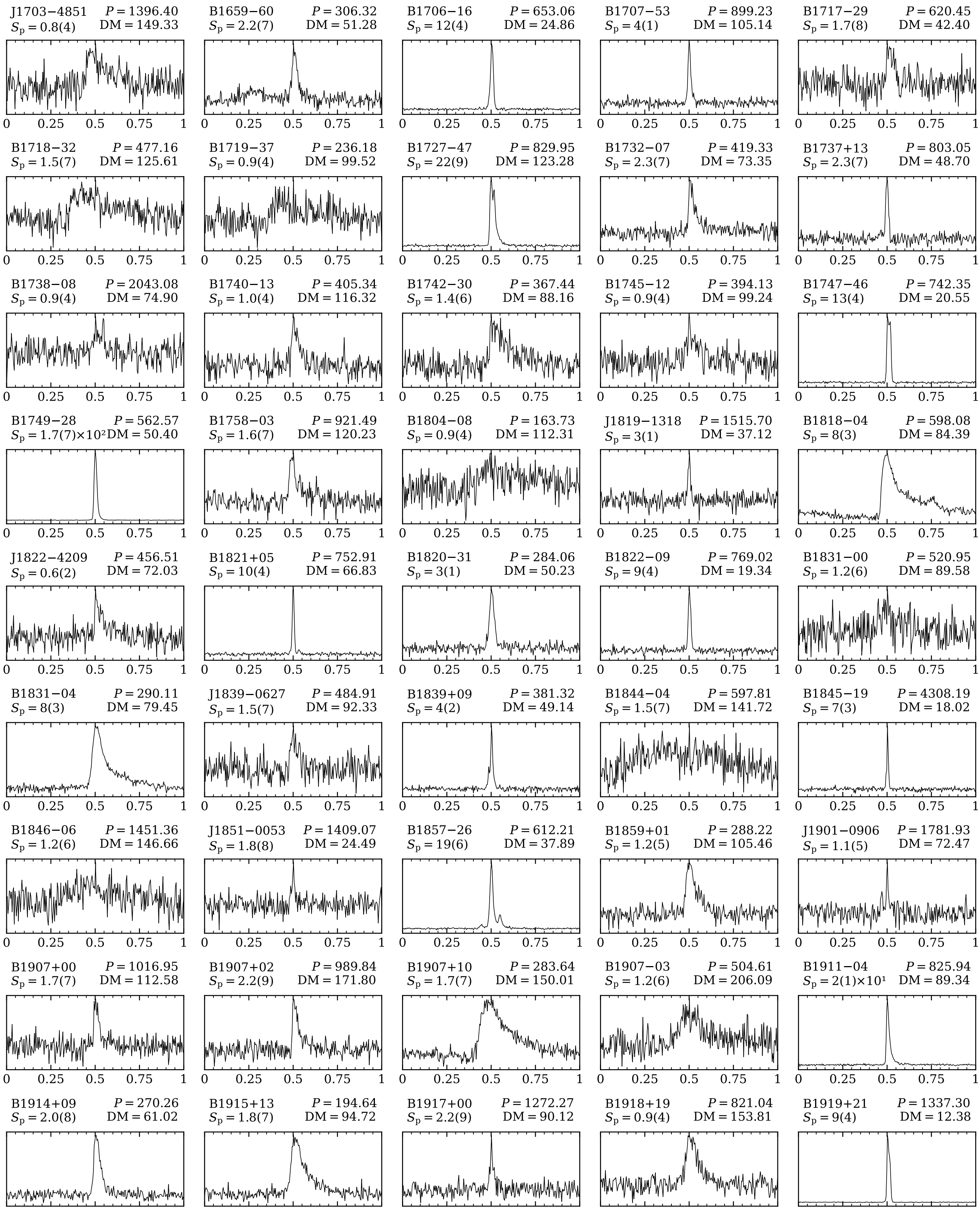

Figure 4. Continued.

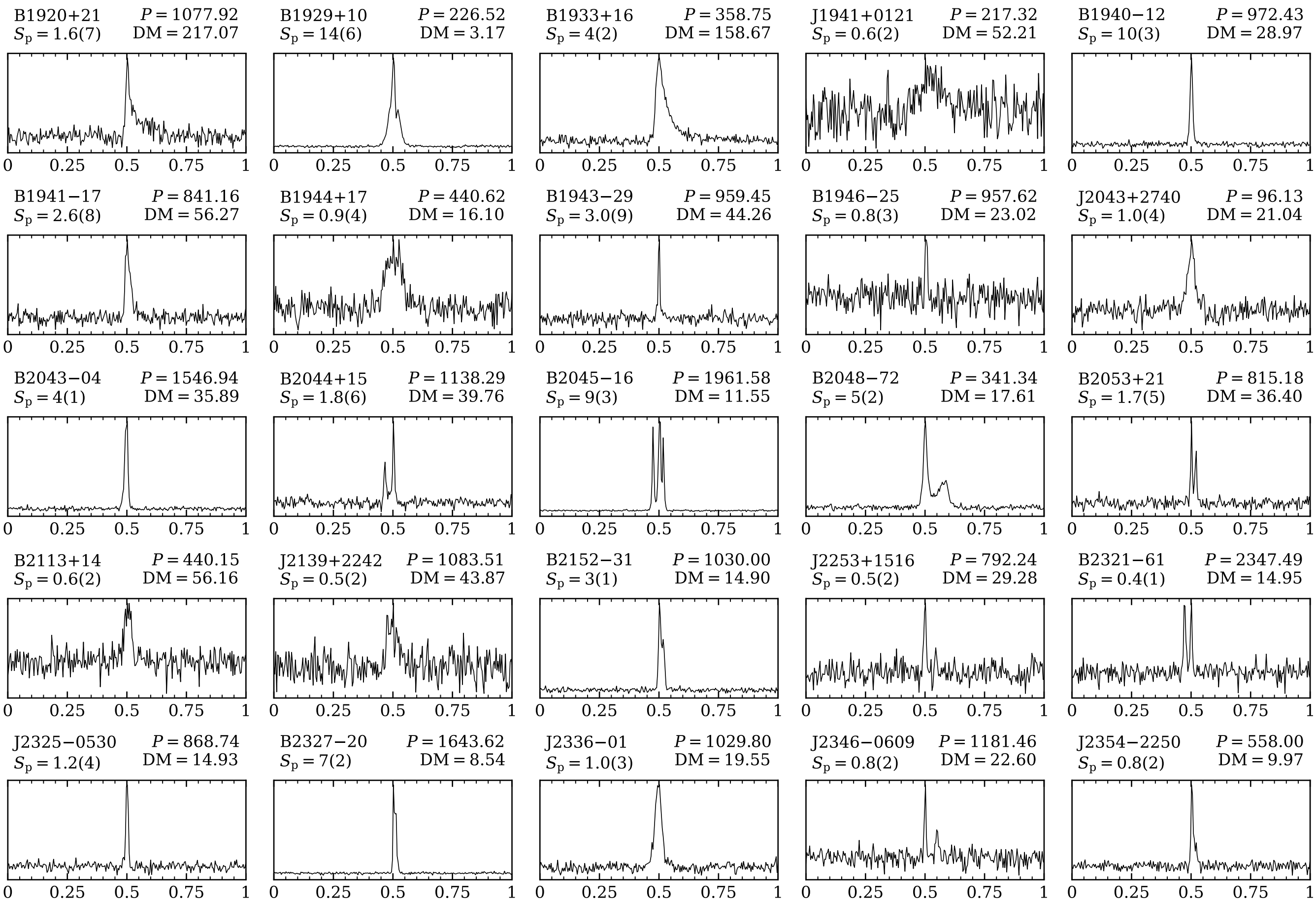

Figure 4. Continued.

For two pulsars (J0514–4408 and J1057–5226), we show the measurements for both the main and interpulse. The remaining measurements are all main pulses. Pulsars with large differences in W_{10} and W_{50} generally fall into two categories: those with significant broadening due to scattering (e.g. B0853–33, B1818–04, B1920+21); and those with multiple profile components with different amplitudes (e.g. B1237+25, B1451–68, B1659–60). The marker colours indicate the DM of each pulsar, which helps to identify which measurements fall into these categories. Since pulsars with higher DMs are generally more scattered, we also observe a bias of higher-DM pulsars generally having larger pulse widths.

Measurements of pulse widths at multiple frequencies can also allow the investigation of the frequency evolution of pulse profiles in attempts to explore the emission geometries or more broadly the frequency dependence of pulsar emission. Pilia et al. (2016) and Kumar et al. (2025) present the related analysis for large pulsar samples at low frequencies with LOFAR and the LWA, spanning 15–167 MHz and 26–88 MHz, respectively. While both studies reveal a general widening of the pulse profiles at lower frequencies, as expected from radius-to-frequency mapping or the birefringence phenomenon, there are many exceptions, and overall there does not appear to be a specific common trend. Further, as acknowledged by Pilia et al. (2016), it is also important to deconvolve scattering tails before meaningful width comparisons are possible at low frequencies. A detailed analysis along these lines, including the comparison with the width estimates at higher frequencies, is therefore deferred to a future publication where we will report the pulse broadening analysis of our MWA sample. Nonetheless, our width estimates are robust and therefore can serve as useful indicators of profile complexity or the degree of pulse broadening, with larger values of the pulse width ratio W_{10}/W_{50} implying either a multi-component pulse profile or dominant scattering tails.

5.2 Flux Densities

Measurements of mean and peak flux densities ($S_{\rm mean}$ and $S_{\rm p}$) obtained using the method described in Section 4.5 are listed in Table 3. We emphasise that these are only first order estimates, as they do not account for any variability due to (refractive) scintillation, and moreover their estimation relies on simulating the beam patterns for telescope performance parameters. Nonetheless, our large sample enables us to infer broader trends in the population, particularly spectral indices and the presence of spectral flattening and turnovers.

In Figure 6, we present a comparison of our flux densities with 22 published measurements from LOFAR (Bilous

https://doi.org/10.1017/pasa.2026.10229

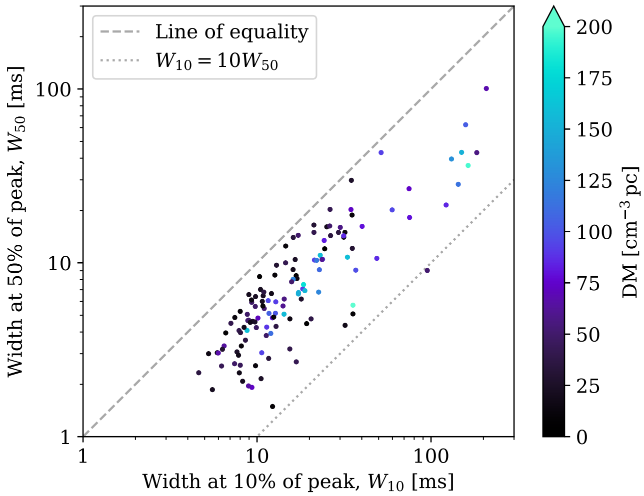

Figure 5. Scatter plot of pulse widths at 10% (W_{10}) and 50% (W_{50}) of the profile peak, for pulsars where both measurements could be made. All measurements come from the main pulse with the exception of PSR B1055–52, for which we compare both the main and interpulse. The dashed and dotted lines show where the widths are equal and where W_{10} is equal to $10W_{50}$. The marker colours show the dispersion measure of each pulsar. Large deviations from equality can be due to either multipath scattering or intrinsic profile structure.

et al. 2016) and 149 from MeerKAT (Keith et al. 2024a). Note that the small overlapping sample with LOFAR is due to their census targeting only northern pulsars. On average, the MWA flux densities are consistent with those from LOFAR, with the outliers likely a result of the aforementioned sources of systematic error (scintillation and calibration). For the detections in common with MeerKAT, we measured two-point power-law spectral indices between the geometric centre frequencies[m] of the MWA and MeerKAT bands (154.02 MHz and 1223.61 MHz, respectively). The spectral indices range from –0.2 to –2.5, with a mean of -1.56 ± 0.13 (standard error) and a standard deviation 0.48. This is slightly shallower than the mean spectral index based on the study of a larger pulsar population, as measured by Jankowski et al. (2018) to be -1.60 ± 0.03 (standard error) with a standard deviation of 0.54 when low and high frequency turnovers are modelled out. This may be due to the lack of commonly-detected pulsars with steep spectral indices (e.g. < –2.0), that may be below the detectable flux density of the MeerKAT observations at *L*-band. The lack of common steep-spectrum pulsars is also reflected in the slightly smaller standard deviation of our sample. It is also possible that the bias is due to some pulsars turning over in the SMART frequency band. However, even if this is the case, the observed bias is small. This may indicate that most pulsars are turning over below 154 MHz, or the pulsars exhibiting significant turnovers in the SMART frequency band were not detected.

There have been several past studies that used low-frequency flux density measurements for exploring the broadband spectra

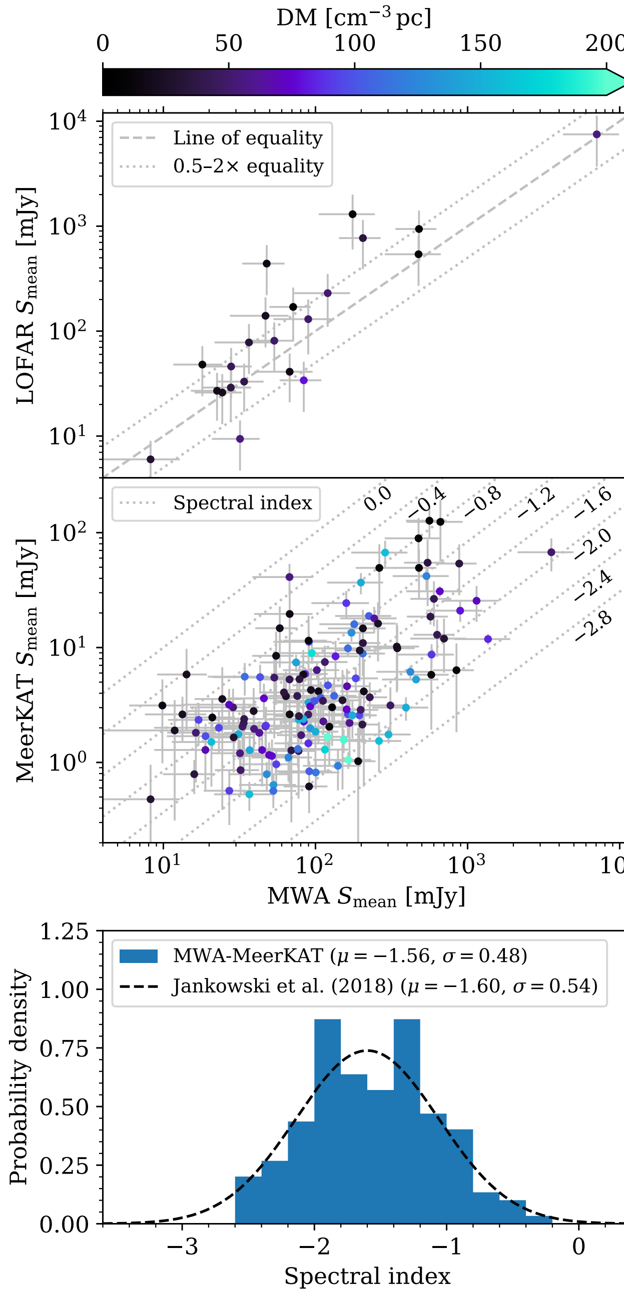

Figure 6. Comparison of the mean flux densities for non-recycled pulsars in SMART data sets (139–170 MHz) with LOFAR mean flux densities (110–188 MHz Bilous et al. 2016) and long-term averaged mean flux densities from the MeerKAT Thousand-Pulsar-Array (MTPA) monitoring program (896–1671 MHz; Keith et al. 2024a). Top: Scatter plot of flux density measurements compared between telescopes. When comparing with LOFAR, we show the line of equality and the factor-of-two error band. When comparing with MeerKAT, we show lines indicating the two-point spectral index. The colour scale shows the dispersion measure of each pulsar. Bottom: Histogram of two-point spectral indices estimated from MWA and MeerKAT flux densities. We also show the mean spectral index distribution of the known pulsar population measured by Jankowski et al. (2018).

m. $\sqrt{\nu_{\rm min}\nu_{\rm max}}$, where $\nu_{\rm min}$ and $\nu_{\rm max}$ are the minimum and maximum frequencies of the observing band.

https://doi.org/10.1017/pasa.2026.10229

of pulsars. Bilous et al. (2016) measured flux densities in the LOFAR high band for 158 pulsars and used them along with those from other published work for performing their spectral fits. LWA measurements (10–88 MHz) have also been used for spectral analysis, though that was for modest samples (Stovall et al. 2015; Kumar et al. 2025). Bilous et al. (2016) used single or broken power-law models for their analysis, which yielded a mean spectral index of −1.4. This is somewhat shallower than the mean value of −1.56 from our analysis and −1.6 from the more comprehensive analysis by Jankowski et al. (2018). Although the geometric centre of the LOFAR frequency band is only ∼10 MHz lower than the SMART band, turnovers in the lower half of the band (i.e. between 110–150 MHz) could significantly lower the band-averaged flux densities. As such, the intriguing discrepancy in mean spectral index may be interpreted as an indication of spectral flattening or turnover below the SMART band. However, as noted by several authors (e.g. Bilous et al. 2016; Jankowski et al. 2018; Bilous et al. 2020), the quality and results from spectral fits generally depend on the number and extent (in frequency coverage) of measurements and their sparsity. The frequency coverage of the data, along with the complexity and diversity of pulsar spectra and the uncertainties inherent to estimating low-frequency flux density measurements from beamformed observations, make the conclusions drawn from our analysis tentative. A more detailed analysis of the spectral characteristics of our southern pulsar sample will hence be instructive, and will be reported in a future publication using the PULSAR_SPECTRA modelling software and catalogue (Swainston, Lee et al. 2022).

5.3 Dispersion and Rotation Measures

Measurements of DM and RM obtained using the methods described in Section 4.3 and Section 4.6 are listed in Table 3. For the sample of non-recycled pulsars, we were able to estimate RMs for 117 pulsars. Thus, including RMs for 25 MSPs reported in Paper III, we have RMs measured for 142 pulsars detected in SMART data sets. For five pulsars (PSRs J0026–1955, J0038–2501, J0418–4154, J0600–5756, and J1612–2408), there are no RM measurements available in the latest pulsar catalogue (v2.7.0; Manchester et al. 2005); for these, we present measurements here for the first time (the locations of these pulsars are shown in Figure 10). For the 112 non-recycled pulsars with RM measurements listed in the pulsar catalogue, Figure 7 shows a plot of our measurements against those from the pulsar catalogue (for a similar comparison of the MSP RMs, see Paper III).

Low-frequency observations provide the advantage of obtaining high-precision estimates of DM and RM. For example, Figure 8 shows our RM uncertainties compared with the catalogued measurements for the same pulsars. The majority of the catalogue measurements (86 out of 112) come from long-term monitoring with MeerKAT (Keith et al. 2024a), which has enabled better precisions than can currently be obtained from single-epoch measurements due to the limited accuracy of global ionospheric models (e.g. a median uncertainty in RM_{ISM} of 0.06 rad m^{-2} for MeerKAT compared with

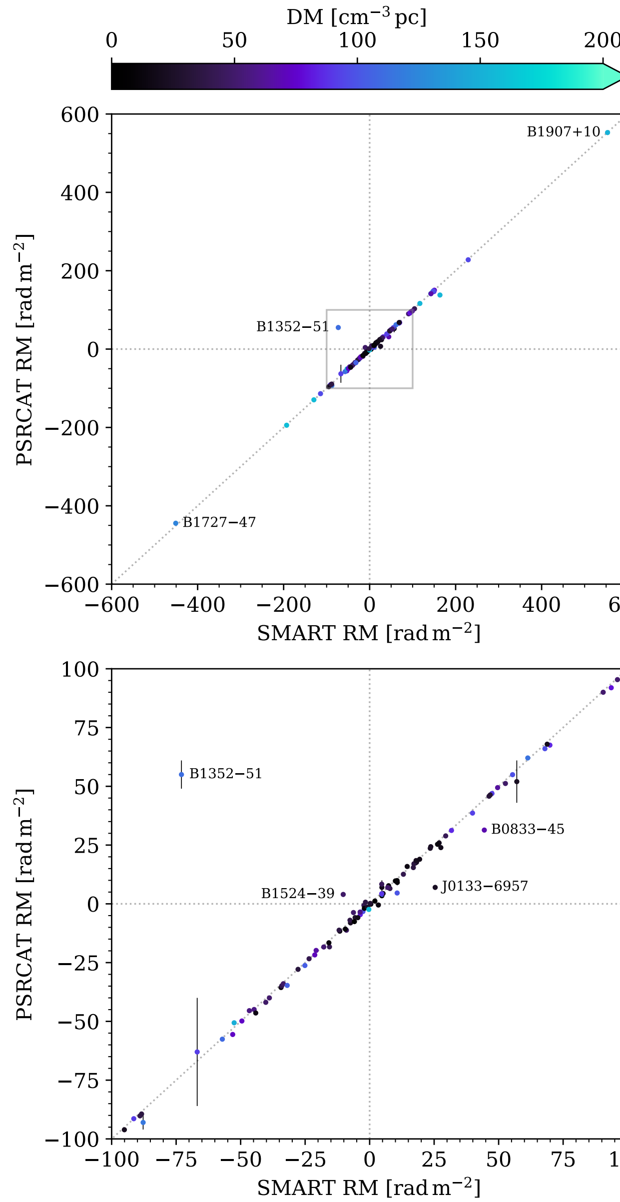

Figure 7. Comparison of RM measurements for non-recycled pulsars in SMART data sets with the RMs reported in the ATNF pulsar catalogue (i.e. PSRCAT; v2.7.0). The top plot shows all pulsars with both MWA and PSRCAT RMs available; the bottom plot shows just those with an RM less than 100 rad m^{-2}, with the corresponding region indicated in the top plot. The highest RMs correspond to PSRs B1727–47 and B1907+10 (annotated), which are both located on the Galactic plane and have DMs of 122.9 cm^{-3} pc and 149.8 cm^{-3} pc, respectively. Several outliers are annotated: PSRs J0133–6957, B0833–45, B1352–51, and B1524–39 (cf. Han, Manchester and Qiao 1999; Johnston et al. 2005; Han et al. 2006).

https://doi.org/10.1017/pasa.2026.10229

0.15 rad m^{-2} for SMART). However, as Figure 8 illustrates, even without long-term monitoring, the precision that we can obtain in the SMART data is often comparable or even better than the best available measurements. For the 29 pulsars that we have obtained more precise RM measurements than reported in the catalogue, we note this in Table 3.

In order to compare and quantify the offsets relative to the published measurements (from the ATNF pulsar catalogue or other published work), we use the z-score of residuals, which is defined as

$$z = \frac{X_{\rm ref} - X_{\rm meas}}{\sqrt{\sigma^2_{\rm ref} + \sigma^2_{\rm meas}}}, \quad (2)$$

where $X_{\rm ref} \pm \sigma_{\rm ref}$ is a reference measurement (e.g. from the pulsar catalogue or published work) and $X_{\rm meas} \pm \sigma_{\rm meas}$ is the measured value from SMART data sets presented in this work. A summary of this is shown in Figure 9 that shows a plot of $z_{\rm DM}$ vs. $z_{\rm RM}$, where $z_{\rm DM}$ and $z_{\rm RM}$ are the z-scores for DM and RM, respectively. This can be used to identify the outliers. For instance, there are handful of cases with $|z_{\rm RM}| > 20$; e.g. for PSR B1352–51 (J1355–5153), our measured RM is -72.6 ± 0.5 rad m^{-2}, compared with 55 ± 6 rad m^{-2} from Han et al. (2006). Our RM measurements generally show a good agreement with those from published work (see Figure 7), and we note that a similar agreement was also noted in the earlier work of Riseley et al. (2020) using image-based measurements (albeit for a much smaller sample). Given that, we are inclined to believe that there may be a sign error in the published RM for B1352–51. A particularly striking case is the Vela pulsar (B0833–45) with $|z_{\rm RM}| > 100$, though this is not surprising in light of recent observational evidence of the presence of small-scale magnetised plasma structure as reported in Lee et al. (2024). These scores can be hence used to identify anomalous sight lines where either discrete and/or magnetised plasma structures are present. In most cases, the outliers in $z_{\rm DM}$ (for which we note those with $|z_{\rm DM}| > 6$) are likely a result of inaccurate DM measurements from past observations (either due to limited S/N or small fractional bandwidths).

A summary of our RM measurements is shown in Figure 10 that shows the Galactic distribution of estimated values for the mean magnetic field strength $\langle B_{\parallel} \rangle$ towards the sight lines. The values are within ± 4 μG, as we may expect for pulsars within the local ISM. A near isotropic distribution of the sample, with a sizeable fraction at high Galactic latitudes, makes them particularly useful in constraining the models for the Galactic magnetic field, both within the halo and the local ISM (e.g. Oswald et al. 2025).

5.4 Pulse Broadening Times

As seen from Figure 4, many of our pulsar profiles show a significant broadening due to scattering in the ISM. A sizeable fraction of these is located at fairly high Galactic latitudes (see Figure 1), where there is currently a paucity of available measurements. These will be invaluable for constraining the model parameters towards the high-latitude regions (Ocker, Cordes and Chatterjee 2020, 2021), which are particularly important for interpreting the measurements of fast radio bursts (FRBs). As well known, at low radio frequencies, many pulsar profiles tend to evolve to complex multi-component shapes. The deconvolution-based approaches (Bhat, Cordes and Chatterjee 2003; Young and Lam 2024) are likely to be more amenable in such cases, rather than traditional forward model approach (Geyer et al. 2017; Krishnakumar et al. 2015). As the deconvolution-based methods make no assumption of the intrinsic pulse shapes, they are likely to yield more reliable estimates of pulse broadening times (Bhat et al. 2004), however the peak signal-to-noise ratio needs to be sufficiently high (S/N $\gtrsim$ 20) for them to converge. They also enable a robust estimation of the pulse broadening function (PBF), and having the PBF shapes accurately determined at multiple well-separated frequencies may also allow for the investigation of the frequency dependence of the PBF – a subtle effect expected when inner scale effects are dominant (cf. Geiger et al. 2025, Cordes et al. submitted). Measuring pulse broadening times and related interpretations are deferred to a future publication, where more data could be combined to increase the S/N.

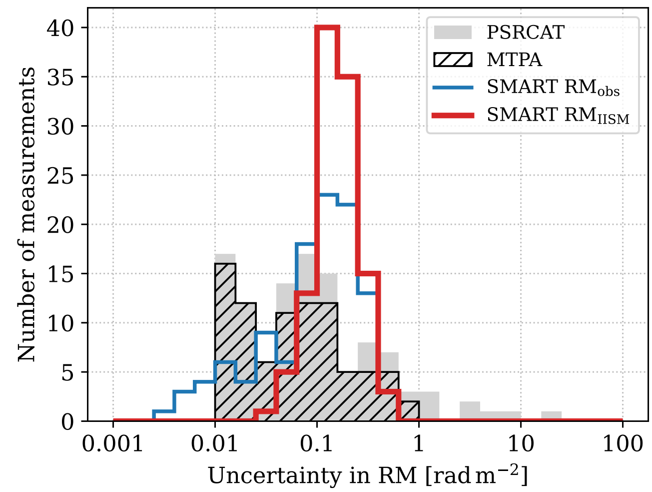

Figure 8. Histograms comparing the uncertainties in RM from this work (before and after ionospheric correction) and the ATNF pulsar catalogue (v2.7.0) for the 112 pulsars with measurements available from both. The subset of catalogue measurements from long-term monitoring with the MeerKAT Thousand Pulsar Array (MTPA; Keith et al. 2024a) are hatched.

6. Discussion and Future Work

With its dense coverage of the entire sky south of +30° in declination, substantial overlaps in survey pointings, and long dwell times (4800 s), SMART datasets present an excellent resource for wide-ranging science. In particular, the novelty in data recording, where unprocessed (voltage) data are recorded (as opposed to channelised time series that has been the norm for all past and ongoing surveys) offers an enormous flexibility, with excellent prospects for science beyond pulsar searches. For instance, comprehensive searches can be performed for transients such as FRBs at uncommonly explored frequencies. A high time resolution imaging pipeline for such applications has just been developed (Di Pietrantonio et al. 2025) and is currently undergoing extensive testing and validation. The data

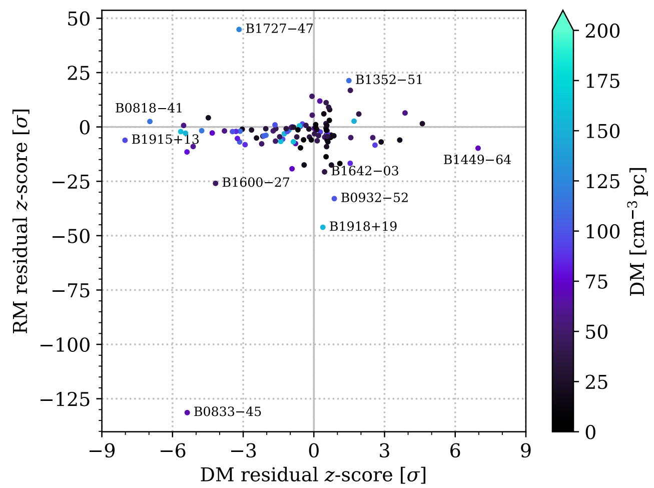

Figure 9. Distribution of residual z-scores (see Equation 2) between the RM and DM estimates from SMART data sets and from the ATNF pulsar catalogue (v2.7.0). Some significant outliers have been annotated.

can also be in principle processed to realise prospective searches for signals of extra-terrestrial intelligence origin. These considerations have prompted the need to secure longer-term archiving for the foreseeable future.

While the primary goal of SMART is to search for new pulsars and fast transients, we also process these data for re-detections of known pulsars in the 140–170 MHz band. With the rapid progression of SKA-Low construction, a reference catalogue of low-frequency detectable pulsars would be an invaluable resource for the science commissioning and verification activities. It is also driven by some of the inherent complexities in processing VCS-recorded data given the data management and computational challenges in handling such large data rates (28–64 TB h^{-1}) and HPC requirements for post-processing. In view of the main intent of this paper, i.e. the release of a low-frequency pulsar catalogue and enhanced data products, we have limited the scope of current analysis primarily to the collation of various measurements and their broad summaries.

Our enhanced data products include: i) pulse profiles and widths, ii) measurements of DMs and RMs, and iii) estimates of (mean and peak) flux densities. For measuring the pulse widths, we have developed a fairly robust method. The measurements of DMs and RMs as such benefit from the strong frequency lever arm provided by our low frequencies, due to which measurement precisions are often times far superior than those obtainable through multi-epoch measurements at high frequencies using more sensitive telescopes. In general, precisions of the order of a fraction of DM unit is easily achievable for most of our detections, and sometimes down to hundredth of a DM unit, even from a single observation. And for RMs, a measurement precision of 0.1 rad m^{-2} is typically achievable, though it is largely limited by our ability to account for ionospheric contribution.

Our flux calibration methodology involves making approximations or assumptions of array beam patterns, which is unavoidable given the complexity of telescope design and array layout. Nonetheless, they are still very useful given the paucity of flux density measurements at these low frequencies for many southern pulsars. Many of our pulsar detections were made at large beam offsets (of the order of a few to several degrees from the primary beam centre; see Table 3) due to the inherent drift-scan nature of SMART observations. Consequently, S/Ns of many of our detections are not a true reflection of the maximum sensitivity achievable with the telescope. These measurements will therefore serve as useful reference for ascertaining the scientific prospects of individual pulsars, especially in the Phase III era when longer and more sensitive pulsar observations become affordable through dedicated targeted observations.

Subsamples of our pulsars were also detected using northern telescopes; of the 205 pulsars detected in SMART data sets, 42 were detected with the LWA and 22 with LOFAR. As discussed in Section 5.2, our flux density measurements can be compared with those from LOFAR and MeerKAT (Bilous et al. 2016; Keith et al. 2024a). In general, DM measurements from LOFAR and LWA (Bilous et al. 2016; Kumar et al. 2025) are significantly more precise than those obtained from our MWA detections. While the combination of a wider bandwidth and a higher sensitivity (at $\delta > 0°$) results in higher precisions for LOFAR DMs, the LWA measurements benefit from a larger frequency lever arm at lower frequencies (and multiple observing epochs). The possibility of frequency-dependent DMs (either due to ISM propagation effects, or unmodelled profile evolution) may also result in measurable changes (offsets) at these low frequencies. For these reasons, detailed comparisons are currently less meaningful for the DM estimates obtained from different low-frequency instruments.

As the processing moves forward we intend to update an electronic version of the catalogue, with the addition of more pulsars as and when they are detected in future processing. This will help to select subsamples of pulsars that are useful for broader ISM studies, besides those that are directly relevant for pulsar timing array (PTA) applications. A substantial fraction (60%) of listed pulsars in Table 3 are located within the local ISM ($\lesssim$3 kpc; DMs $\lesssim$60 cm^{-3} pc); regular monitoring of these pulsars can thus facilitate a detailed characterisation and modelling of the local ISM in which most PTA pulsars are located (Shannon et al. 2025). A multi-year time baseline of such pulsars sampling many sight lines can help to build a tomographic view of the local ISM, in an effort to improve the ISM noise modelling for PTAs, and to better quantify the ISM noise budget in timing data sets. Another aspect of direct relevance in this context is an improved modelling of the solar wind, which can benefit from regular monitoring of pulsars (both MSPs and longer period pulsars) closer to the ecliptic (Susarla et al. 2025). In general, regular observations of large pulsar samples (at PTA-like cadence) will prove beneficial for probing the ISM at physical scales ($\sim$1–10 au) that are inaccessible to other observational probes.

https://doi.org/10.1017/pasa.2026.10229

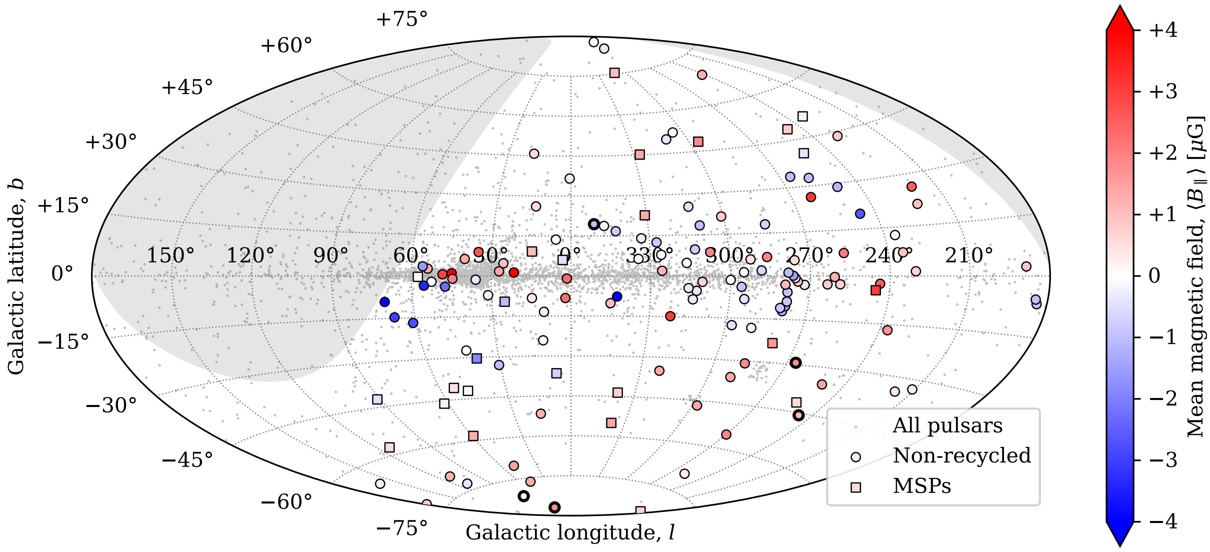

Figure 10. Galactic distribution of the line-of-sight component of the mean magnetic field $\langle B_{\parallel} \rangle$, estimated for a sample of 117 non-recycled pulsars (circles; from this work) and 25 MSPs (squares; from Paper III) using the RM and DM measurements deduced from SMART data sets. The pulsars with RMs measured for the first time in this work are emphasised. The grey dots show all pulsars from the ATNF pulsar catalogue (v2.7.0). Declinations above $+30^{\circ}$, which are out of reach of the MWA, are shaded in grey.

7. Summary

The successful completion of data collection marks a significant milestone for the SMART project, which will emerge as the most comprehensive and sensitive pulsar survey in the southern skies in the frequency band of SKA-Low. The 4 PB of data collected through this project essentially captures the high-time resolution sky in the pristine low-frequency band for the southern skies. Motivated by the SKA-Low development towards science commissioning and verification, and wide-ranging science benefits provided by low-frequency measurements, we have embarked on a systematic processing of the full datasets and making the pulsar detections and enhanced data products accessible for the wider science community. Our processing has resulted in the detection of 245 pulsars including the 40 MSPs reported in Paper III. Along with the 25 new pulsar discoveries from the searches so far, this will effectively constitute our first data release SMART DR1.

Our measured pulse profiles in the 140–170 MHz band are particularly valuable as the first high-fidelity records (i.e. an atlas) of a sizeable sample of southern pulsar detections at these uncommonly observed frequencies. We provide robust estimates of pulse widths at 10% and 50% of pulse peak (i.e. W_{10} and W_{50}, respectively), which may serve as useful indicators of profile complexity or measurable pulse broadening. We also provide high-precision measurements of RMs for 142 pulsars, a significant fraction of which is located away from the plane ($|b| \gtrsim 5^{\circ}$) and hence will be useful to constrain or improve the models for the Galactic magnetic field. Although our measured flux densities (at 154 MHz) are only first-order estimates (as we do not account for scintillation variability), they are still valuable for spectral analysis, considering the poorly explored pulsar spectra at these lower frequencies.

We provide a range of data products, including multi-channel pulse profiles, folded profiles over short sub-integrations, and measurements of DMs, RMs, and flux densities. The overlap in the SMART survey pointings is especially a major advantage, and can be leveraged for multiple detections of a pulsar, which can then be co-added for improved detections and better pulse profiles, and to obtain more reliable measurements of flux densities. In general, we have chosen the best available detection (maximum S/N) for this release, and as the processing moves forward, we intend to periodically update our data products and pulsar detections.

Acknowledgements. We thank the anonymous reviewer for several useful comments that helped to improve the content and presentation of this paper. This scientific work made use of data obtained from Inyarrimanha Ilgari Bundara, the CSIRO Murchison Radio-astronomy Observatory. We acknowledge the Wajarri Yamaji People as the Traditional Owners and Native Title Holders of the Observatory site. Support for the operation of the MWA is provided by the Australian Government (NCRIS), under a contract to Curtin University administered by Astronomy Australia Limited (AAL). CPL is supported by an Australian Government Research Training Program (RTP) Stipend and RTP Fee-Offset Scholarship (https://doi.org/10.82133/C42F-K220). MX and QF are supported by the National SKA Program of China (2025SKA0160100). This work was supported by resources provided by the Pawsey Supercomputing Research Centre's Setonix Supercomputer (https://doi.org/10.48569/18sb-8s43), and their Acacia (https://doi.org/10.48569/nfe9-a426) and Banksia (https://doi.org/10.48569/tnja-4s30) Object Storage systems, with funding from the Australian Government and the Government of Western Australia. This work was also supported by resources awarded under AAL's ASTAC merit allocation scheme on the OzSTAR national facility at the Swinburne University of Technology. The OzSTAR program receives funding in part from the Astronomy National Collaborative Research Infrastructure Strategy (NCRIS) allocation provided by the Australian Government.

https://doi.org/10.1017/pasa.2026.10229

Software. We acknowledge the use of the following software and packages for this work: MWA_HYPERDRIVE (Jordan et al. 2025), CASA (McMullin et al. 2007), DSPSR (van Straten and Bailes 2010, 2011), PRESTO (Ransom 2001; Ransom 2011), PSRCHIVE (Hotan, van Straten and Manchester 2004; van Straten et al. 2011), TEMPO2 (Hobbs, Edwards and Manchester 2006; Hobbs and Edwards 2012), PINT (Luo et al. 2019; Luo et al. 2021), PSRPOPPY (Bates et al. 2014), NEXTFLOW (Di Tommaso et al. 2017), NUMPY (Harris et al. 2020), SCIPY (Virtanen et al. 2020), ASTROPY (Astropy Collaboration et al. 2013; Astropy Collaboration et al. 2018; Astropy Collaboration et al. 2022), PSRQPY (Pitkin 2018), SPINIFEX (Mevius, Thomson and Dijkema 2025).

Data Availability. The full-polarisation folded archives for the detected pulsars are available in PSRFITS format with 256 phase bins, 30-s subintegrations, and 40-kHz frequency resolution. The pulse profiles are also available in ASCII format. We have also provided the data from Tables 2 and 3 in a machine-readable format. The dataset can be accessed under the DOI: 10.5281/zenodo.20064197.

References

Astropy Collaboration, A. M. Price-Whelan, B. M. Sipőcz, H. M. Günther, P. L. Lim, S. M. Crawford, S. Conseil et al. 2018. The Astropy Project: Building an Open-science Project and Status of the v2.0 Core Package. AJ 156, no. 3 (September): 123. https://doi.org/10.3847/1538-3881/aabc4f. arXiv: 1801.02634 [astro-ph.IM].

Astropy Collaboration, Adrian M. Price-Whelan, Pey Lian Lim, Nicholas Earl, Nathaniel Starkman, Larry Bradley, David L. Shupe et al. 2022. The Astropy Project: Sustaining and Growing a Community-oriented Open-source Project and the Latest Major Release (v5.0) of the Core Package. ApJ 935, no. 2 (August): 167. https://doi.org/10.3847/1538-4357/ac7c74. arXiv: 2206.14220 [astro-ph.IM].

Astropy Collaboration, Thomas P. Robitaille, Erik J. Tollerud, Perry Greenfield, Michael Droettboom, Erik Bray, Tom Aldcroft et al. 2013. Astropy: A community Python package for astronomy. A&A 558 (October): A33. https://doi.org/10.1051/0004-6361/201322068. arXiv: 1307.6212 [astro-ph.IM].

Bates, S. D., D. R. Lorimer, A. Rane and J. Swiggum. 2014. PSRPOPPY: An open-source package for pulsar population simulations. MNRAS 439 (3): 2893–2902. ISSN: 13652966. https://doi.org/10.1093/mnras/stu157. arXiv: 1311.3427.

Bhat, N. D. R., J. M. Cordes and S. Chatterjee. 2003. A CLEAN-based Method for Deconvolving Interstellar Pulse Broadening from Radio Pulses. ApJ 584, no. 2 (February): 782–790. https://doi.org/10.1086/345775. arXiv: astro-ph/0207451 [astro-ph].

Bhat, N. D. R., N. A. Swainston, S. J. McSweeney, M. Xue, B. W. Meyers, S. Kudale, S. Dai et al. 2023a. The Southern-sky MWA Rapid Two-metre (SMART) pulsar survey—I. Survey design and processing pipeline. PASA 40 (May): e021. https://doi.org/10.1017/pasa.2023.17. arXiv: 2302.11911 [astro-ph.HE].

———. 2023b. The Southern-sky MWA Rapid Two-metre (SMART) pulsar survey—II. Survey status, pulsar census, and first pulsar discoveries. PASA 40 (May): e020. https://doi.org/10.1017/pasa.2023.18. arXiv: 2302.11920 [astro-ph.HE].

Bhat, N. D. Ramesh, James M. Cordes, Fernando Camilo, David J. Nice and Duncan R. Lorimer. 2004. Multifrequency Observations of Radio Pulse Broadening and Constraints on Interstellar Electron Density Microstructure. ApJ 605, no. 2 (April): 759–783. https://doi.org/10.1086/382680. arXiv: astro-ph/0401067 [astro-ph].

Bhatnagar, S. and R. Nityananda. 2001. Solving for closure errors due to polarization leakage in radio interferometry of unpolarized sources. A&A 375 (August): 344–350. https://doi.org/10.1051/0004-6361:20010799. arXiv: astro-ph/0106348 [astro-ph].

Bilous, A. V., L. Bondonneau, V. I. Kondratiev, J.-M. Grießmeier, G. Theureau, J. W. T. Hessels, M. Kramer et al. 2020. A LOFAR census of non-recycled pulsars: extending to frequencies below 80 MHz. A&A 635 (March): A75. https://doi.org/10.1051/0004-6361/201936627. arXiv: 1909.01607 [astro-ph.HE].

Bilous, A. V., V. I. Kondratiev, M. Kramer, E. F. Keane, J. W. T. Hessels, B. W. Stappers, V. M. Malofeev et al. 2016. A LOFAR census of non-recycled pulsars: average profiles, dispersion measures, flux densities, and spectra. A&A 591 (June): A134. https://doi.org/10.1051/0004-6361/201527702. arXiv: 1511.01767 [astro-ph.SR].

Brentjens, M. A. and A. G. de Bruyn. 2005. Faraday rotation measure synthesis. A&A 441, no. 3 (October): 1217–1228. https://doi.org/10.1051/0004-6361:20052990. arXiv: astro-ph/0507349 [astro-ph].

Cordes, J. M. and T. J. W. Lazio. 2002. NE2001.I. A New Model for the Galactic Distribution of Free Electrons and its Fluctuations. *arXiv e-prints* (July): astro-ph/0207156. arXiv: astro-ph/0207156 [astro-ph].

Cordes, J. M., R. M. Shannon and D. R. Stinebring. 2016. Frequency-dependent Dispersion Measures and Implications for Pulsar Timing. ApJ 817, no. 1 (January): 16. https://doi.org/10.3847/0004-637X/817/1/16. arXiv: 1503.08491 [astro-ph.IM].

Di Pietrantonio, Cristian, Marcin Sokolowski, Christopher Harris, Daniel Price and Randall Wayth. 2025. BLINK: An end-to-end GPU high time resolution imaging pipeline for fast radio burst searches with the Murchison Widefield Array. PASA 42 (May): e074. https://doi.org/10.1017/pasa.2025.10043. arXiv: 2505.15204 [astro-ph.IM].

Di Tommaso, P., M. Chatzou, E. Floden, P. Prieto Barja, E. Palumbo and C. Notredame. 2017. Nextflow enables reproducible computational workflows. *Nature Biotechnology* 35 (April): 316–319. https://doi.org/10.1038/nbt.3820.

Dierckx, P. 1975. An algorithm for smoothing, differentiation and integration of experimental data using spline functions. *Journal of Computational and Applied Mathematics* 1 (3): 165–184. ISSN: 0377-0427. https://doi.org/https://doi.org/10.1016/0771-050X(75)90034-0. https://www.sciencedirect.com/science/article/pii/0771050X75900340.

Geiger, Abra, James M. Cordes, Michael T. Lam, Stella Koch Ocker, Shami Chatterjee, Zaven Arzoumanian, Ava L. Battaglia et al. 2025. The NANOGrav 12.5 yr Data Set: Probing Interstellar Turbulence and Precision Pulsar Timing with PSR J1903+0327. ApJ 986, no. 2 (June): 191. https://doi.org/10.3847/1538-4357/add0b6. arXiv: 2411.08191 [astro-ph.HE].

Geyer, M., A. Karastergiou, V. I. Kondratiev, K. Zagkouris, M. Kramer, B. W. Stappers, J. -M. Grießmeier et al. 2017. Scattering analysis of LOFAR pulsar observations. MNRAS 470, no. 3 (September): 2659–2679. https://doi.org/10.1093/mnras/stx1151. arXiv: 1706.04205 [astro-ph.HE].

Grover, Garvit, N. D. Ramesh Bhat, Samuel J. McSweeney, Christopher P. Lee, Bradley W. Meyers, Chia Min Tan and Sanjay S. Kudale. 2024. Discovery and Follow-up of a Quasiperiodically Nulling and Subpulse Drifting Pulsar with the Murchison Widefield Array. ApJ 970, no. 1 (July): 78. https://doi.org/10.3847/1538-4357/ad509e. arXiv: 2405.16725 [astro-ph.HE].

Han, J. L., R. N. Manchester, A. G. Lyne, G. J. Qiao and W. van Straten. 2006. Pulsar Rotation Measures and the Large-Scale Structure of the Galactic Magnetic Field. ApJ 642, no. 2 (May): 868–881. https://doi.org/10.1086/501444. arXiv: astro-ph/0601357 [astro-ph].

Han, J. L., R. N. Manchester and G. J. Qiao. 1999. Pulsar rotation measures and the magnetic structure of our Galaxy. MNRAS 306, no. 2 (June): 371–380. https://doi.org/10.1046/j.1365-8711.1999.02544.x. arXiv: astro-ph/9903101 [astro-ph].

Harris, Charles R., K. Jarrod Millman, Stéfan J. van der Walt, Ralf Gommers, Pauli Virtanen, David Cournapeau, Eric Wieser et al. 2020. Array programming with NumPy. Nature 585, no. 7825 (September): 357–362. https://doi.org/10.1038/s41586-020-2649-2. arXiv: 2006.10256 [cs.MS].

Hassall, T. E., B. W. Stappers, J. W. T. Hessels, M. Kramer, A. Alexov, K. Anderson, T. Coenen et al. 2012. Wide-band simultaneous observations of pulsars: disentangling dispersion measure and profile variations. A&A 543 (July): A66. https://doi.org/10.1051/0004-6361/201218970. arXiv: 1204.3864 [astro-ph.HE].

Hobbs, G. B., R. T. Edwards and R. N. Manchester. 2006. TEMPO2, a new pulsar-timing package - I. An overview. MNRAS 369, no. 2 (June): 655–672. https://doi.org/10.1111/j.1365-2966.2006.10302.x. arXiv: astro-ph/0603381 [astro-ph].

Hobbs, George and Russell Edwards. 2012. *Tempo2: Pulsar Timing Package.* Astrophysics Source Code Library, record ascl:1210.015, October. ascl: 1210.015.

Hotan, A. W., W. van Straten and R. N. Manchester. 2004. PSRCHIVE and PSRFITS: An Open Approach to Radio Pulsar Data Storage and Analysis. PASA 21, no. 3 (January): 302–309. https://doi.org/10.1071/AS04022. arXiv: astro-ph/0404549 [astro-ph].

Jankowski, F., W. van Straten, E. F. Keane, M. Bailes, E. D. Barr, S. Johnston and M. Kerr. 2018. Spectral properties of 441 radio pulsars. MNRAS 473, no. 4 (February): 4436–4458. https://doi.org/10.1093/mnras/stx2476. arXiv: 1709.08864 [astro-ph.HE].

Johnston, Simon, G. Hobbs, S. Vigeland, M. Kramer, J. M. Weisberg and A. G. Lyne. 2005. Evidence for alignment of the rotation and velocity vectors in pulsars. MNRAS 364, no. 4 (December): 1397–1412. https://doi.org/10.1111/j.1365-2966.2005.09669.x. arXiv: astro-ph/0510260 [astro-ph].

Jordan, Christopher H., Dev Null, Cathryn M. Trott, Jack L. B. Line, J. Kariuki Chege, Christene R. Lynch, Chuneeta D. Nunhokee, Greg Sleap and Randall B. Wayth. 2025. MWA_HYPERDRIVE: Next generation calibration software for the Murchison Widefield Array radio telescope. In *2025 URSI Asia-Pacific Radio Science Meeting (AP-RASC),* 1–4. https://doi.org/10.46620/URSIAPRASC25/LSCN1310.

Kaur, D., N. D. R. Bhat, S. E. Tremblay, R. M. Shannon, S. J. McSweeney, S. M. Ord, A. P. Beardsley et al. 2019. A High Time-resolution Study of the Millisecond Pulsar J2241-5236 at Frequencies Below 300 MHz. ApJ 882, no. 2 (September): 133. https://doi.org/10.3847/1538-4357/ab338f. arXiv: 1907.08916 [astro-ph.HE].

Kaur, Dilpreet, N. D. Ramesh Bhat, Shi Dai, Samuel J. McSweeney, Ryan M. Shannon, Sanjay Kudale and Willem van Straten. 2022. Detection of Frequency-dependent Dispersion Measure toward the Millisecond Pulsar J2241-5236 from Contemporaneous Wideband Observations. ApJ 930, no. 2 (May): L27. https://doi.org/10.3847/2041-8213/ac64ff. arXiv: 2204.07973 [astro-ph.HE].

Keane, E., B. Bhattacharyya, M. Kramer, B. Stappers, E. F. Keane, B. Bhattacharyya, M. Kramer et al. 2015. A Cosmic Census of Radio Pulsars with the SKA. In *Advancing astrophysics with the square kilometre array (aaska14),* 40. April. arXiv: 1501.00056 [astro-ph.IM].

Keane, Evan F., Vanessa Graber, Lina Levin, Chia Min Tan, Owen A. Johnson, Cherry Ng, Celsa Pardo-Araujo, Michele Ronchi, Dany Vohl and Mengyao Xue. 2025. A Square Kilometre Array Pulsar Census. *The Open Journal of Astrophysics* 8 (December): 54256. https://doi.org/10.33232/001c.154256. arXiv: 2512.16153 [astro-ph.HE].

Keith, M. J., A. Jameson, W. van Straten, M. Bailes, S. Johnston, M. Kramer, A. Possenti et al. 2010. The High Time Resolution Universe Pulsar Survey - I. System configuration and initial discoveries. MNRAS 409, no. 2 (December): 619–627. https://doi.org/10.1111/j.1365-2966.2010.17325.x. arXiv: 1006.5744 [astro-ph.HE].

Keith, M. J., S. Johnston, A. Karastergiou, P. Weltevrede, M. E. Lower, A. Basu, B. Posselt et al. 2024a. The Thousand-Pulsar-Array programme on MeerKAT - XIII. Timing, flux density, rotation measure, and dispersion measure time series of 597 pulsars. MNRAS 530, no. 2 (May): 1581–1591. https://doi.org/10.1093/mnras/stae937. arXiv: 2404.02051 [astro-ph.HE].

Keith, M. J., Simon Johnston, Aris Karastergiou, Patrick Weltevrede, Marcus Lower, Avishek Basu, Bettina Posselt et al. 2024b. *MeerTime Thousand Pulsar Array Data Release,* April. https://doi.org/10.5281/zenodo.8430591. https://doi.org/10.5281/zenodo.8430591.

Krishnakumar, M. A., D. Mitra, A. Naidu, B. C. Joshi and P. K. Manoharan. 2015. Scatter Broadening Measurements of 124 Pulsars At 327 Mhz. ApJ 804, no. 1 (May): 23. https://doi.org/10.1088/0004-637X/804/1/23. arXiv: 1501.05401 [astro-ph.HE].

Kumar, P., G. B. Taylor, K. Stovall, J. Dowell and S. M. White. 2025. A Multifrequency Census of 100 Pulsars below 100 MHz with LWA: A Systematic Study of Flux Density, Spectra, Timing, Dispersion, Polarization, and Its Variation from a Decade of Observations. ApJ 982, no. 2 (April): 132. https://doi.org/10.3847/1538-4357/adb97a. arXiv: 2501.11862 [astro-ph.HE].

Kumar, Pratik, Marcin Sokolowski and Randall Wayth. 2026. A 50–250 MHz Pulsar Census with an SKA-Low Prototype Station: Spectra and Polarization. ApJS 283, no. 2 (April): 61. https://doi.org/10.3847/1538-4365/ae4744. arXiv: 2603.11553 [astro-ph.HE].

Lee, C. P., N. D. R. Bhat, B. W. Meyers, S. J. McSweeney, W. van Straten, C. M. Tan, M. Xue et al. 2025. The Southern-sky MWA Rapid Two-metre (SMART) pulsar survey—III. A census of millisecond pulsars at 154 MHz. PASA 42 (September): e117. https://doi.org/10.1017/pasa.2025.10081. arXiv: 2508.10330 [astro-ph.HE].

Lee, C. P., N. D. R. Bhat, M. Sokolowski, B. W. Meyers and A. Magro. 2024. Probing magneto-ionic microstructure towards the Vela pulsar using a prototype SKA-Low station. PASA 41 (October): e080. https://doi.org/10.1017/pasa.2024.71. arXiv: 2411.00602 [astro-ph.HE].

Lee, C. P., N. D. R. Bhat, M. Sokolowski, N. A. Swainston, D. Ung, A. Magro and R. Chiello. 2022. Spectral analysis of 22 radio pulsars using SKA-Low precursor stations. PASA 39 (September): e042. https://doi.org/10.1017/pasa.2022.40. arXiv: 2208.07182 [astro-ph.HE].

Luo, Jing, Scott Ransom, Paul Demorest, Paul S. Ray, Anne Archibald, Matthew Kerr, Ross J. Jennings et al. 2021. PINT: A Modern Software Package for Pulsar Timing. ApJ 911, no. 1 (April): 45. https://doi.org/10.3847/1538-4357/abe62f. arXiv: 2012.00074 [astro-ph.IM].

Luo, Jing, Scott Ransom, Paul Demorest, Rutger van Haasteren, Paul Ray, Kevin Stovall, Matteo Bachetti et al. 2019. *PINT: High-precision pulsar timing analysis package.* Astrophysics Source Code Library, record ascl:1902.007, February. ascl: 1902.007.

Macario, Giulia, Giuseppe Pupillo, Gianni Bernardi, Pietro Bolli, Paola Di Ninni, Giovanni Comoretto, Andrea Mattana et al. 2022. Characterization of the SKA1-Low prototype station Aperture Array Verification System 2. *Journal of Astronomical Telescopes, Instruments, and Systems* 8 (January): 011014. https://doi.org/10.1117/1.JATIS.8.1.011014. arXiv: 2109.11983 [astro-ph.IM].

Malofeev, V. M., O. I. Malov and N. V. Shchegoleva. 2000. Flux Densities of 235 Pulsars at 102.5 MHz. *Astronomy Reports* 44, no. 7 (July): 436–445. https://doi.org/10.1134/1.163868.

Manchester, R. N., G. B. Hobbs, A. Teoh and M. Hobbs. 2005. The Australia Telescope National Facility Pulsar Catalogue. AJ 129, no. 4 (April): 1993–2006. https://doi.org/10.1086/428488. arXiv: astro-ph/0412641 [astro-ph].

Manchester, R. N., A. G. Lyne, F. Camilo, J. F. Bell, V. M. Kaspi, N. D'Amico, N. P. F. McKay et al. 2001. The Parkes multi-beam pulsar survey - I. Observing and data analysis systems, discovery and timing of 100 pulsars. MNRAS 328, no. 1 (November): 17–35. https://doi.org/10.1046/j.1365-8711.2001.04751.x. arXiv: astro-ph/0106522 [astro-ph].

Manchester, R. N., A. G. Lyne, N. D'Amico, M. Bailes, S. Johnston, D. R. Lorimer, P. A. Harrison, L. Nicastro and J. F. Bell. 1996. The Parkes Southern Pulsar Survey. I. Observing and data analysis systems and initial results. MNRAS 279, no. 4 (April): 1235–1250. https://doi.org/10.1093/mnras/279.4.1235.

McMullin, J. P., B. Waters, D. Schiebel, W. Young and K. Golap. 2007. CASA Architecture and Applications. In *Astronomical data analysis software and systems xvi,* edited by R. A. Shaw, F. Hill and D. J. Bell, 376:127. Astronomical Society of the Pacific Conference Series. October.

McSweeney, S. J., S. M. Ord, D. Kaur, N. D. R. Bhat, B. W. Meyers, S. E. Tremblay, J. Jones, B. Crosse and K. R. Smith. 2020. MWA tied-array processing III: Microsecond time resolution via a polyphase synthesis filter. PASA 37 (January): e034. https://doi.org/10.1017/pasa.2020.24. arXiv: 2007.03171 [astro-ph.IM].

McSweeney, Samuel J., N. D. Ramesh Bhat, Nicholas A. Swainston, Keegan R. Smith, Sanjay Kudale, Paul Hancock, Willem van Straten et al. 2022. Independent Discovery of a Nulling Pulsar with Unusual Subpulse Drifting Properties with the Murchison Widefield Array. ApJ 933, no. 2 (July): 210. https://doi.org/10.3847/1538-4357/ac75bc. arXiv: 2206.00805 [astro-ph.HE].

Mcsweeney, Samuel J., Jared Moseley, Natasha Hurley-Walker, Garvit Grover, Csanád Horváth, Timothy J. Galvin, Bradley W. Meyers and Chia Min Tan. 2025. Discovery of an RRAT-like Pulsar via Its Single Pulses in a Murchison Widefield Array Imaging Survey. ApJ 981, no. 2 (March): 143. https://doi.org/10.3847/1538-4357/adb27f. arXiv: 2502.02130 [astro-ph.HE].

Mevius, Maaijke, Alec Thomson and Tammo Jan Dijkema. 2025. *Spinifex.* V. 1.0, March. https://doi.org/10.5281/zenodo.15000430. https://doi.org/10.5281/zenodo.15000430.

Meyers, B. W., S. E. Tremblay, N. D. R. Bhat, R. M. Shannon, F. Kirsten, M. Sokolowski, S. J. Tingay, S. I. Oronsaye and S. M. Ord. 2017. Spectral Flattening at Low Frequencies in Crab Giant Pulses. ApJ 851, no. 1 (December): 20. ISSN: 1538-4357. https://doi.org/10.3847/1538-4357/aa8bba. https://iopscience.iop.org/article/10.3847/1538-4357/aa8bba.

Mitchell, D. A., L. J. Greenhill, R. B. Wayth, R. J. Sault, C. J. Lonsdale, R. J. Cappallo, M. F. Morales and S. M. Ord. 2008. Real-Time Calibration of the Murchison Widefield Array. *IEEE Journal of Selected Topics in Signal Processing* 2, no. 5 (November): 707–717. https://doi.org/10.1109/JSTSP.2008.2005327.

Morello, V., E. D. Barr, S. Cooper, M. Bailes, S. Bates, N. D. R. Bhat, M. Burgay et al. 2019. The High Time Resolution Universe survey - XIV. Discovery of 23 pulsars through GPU-accelerated reprocessing. MNRAS 483, no. 3 (March): 3673–3685. https://doi.org/10.1093/mnras/sty3328. arXiv: 1811.04929 [astro-ph.IM].

Morrison, I. S., B. Crosse, G. Sleap, R. B. Wayth, A. Williams, M. Johnston-Hollitt, J. Jones, S. J. Tingay, M. Walker and L. Williams. 2023. MWAX: A new correlator for the Murchison Widefield Array. PASA 40 (April): e019. https://doi.org/10.1017/pasa.2023.15. arXiv: 2303.11557 [astro-ph.IM].

Ocker, S. K. and J. M. Cordes. 2026. NE2025: An Updated Electron Density Model for the Galactic Interstellar Medium. *arXiv e-prints* (February): arXiv:2602.11838. https://doi.org/10.48550/arXiv.2602.11838. arXiv: 2602.11838 [astro-ph.GA].

Ocker, Stella Koch, James M. Cordes and Shami Chatterjee. 2020. Electron Density Structure of the Local Galactic Disk. ApJ 897, no. 2 (July): 124. https://doi.org/10.3847/1538-4357/ab98f9. arXiv: 2004.11921 [astro-ph.GA].

———. 2021. Constraining Galaxy Halos from the Dispersion and Scattering of Fast Radio Bursts and Pulsars. ApJ 911, no. 2 (April): 102. https://doi.org/10.3847/1538-4357/abeb6e. arXiv: 2101.04784 [astro-ph.GA].

Ord, S. M., S. E. Tremblay, S. J. McSweeney, N. D. R. Bhat, C. Sobey, D. A. Mitchell, P. J. Hancock and F. Kirsten. 2019. MWA tied-array processing I: Calibration and beamformation. PASA 36 (August): e030. https://doi.org/10.1017/pasa.2019.17. arXiv: 1905.01826 [astro-ph.IM].

Oswald, L. S., P. Weltevrede, B. Posselt, S. Johnston, A. Karastergiou and M. E. Lower. 2025. The Thousand-Pulsar-Array programme on MeerKAT—XVI. Mapping the Galactic magnetic field with pulsar observations. MNRAS 540, no. 3 (July): 2112–2130. https://doi.org/10.1093/mnras/staf645. arXiv: 2504.09722 [astro-ph.GA].

Pilia, M., J. W. T. Hessels, B. W. Stappers, V. I. Kondratiev, M. Kramer, J. van Leeuwen, P. Weltevrede et al. 2016. Wide-band, low-frequency pulse profiles of 100 radio pulsars with LOFAR. A&A 586 (February): A92. https://doi.org/10.1051/0004-6361/201425196. arXiv: 1509.06396 [astro-ph.HE].

Pitkin, M. 2018. psrqpy: a python interface for querying the ATNF pulsar catalogue. *Journal of Open Source Software* 3, no. 22 (February): 538. https://doi.org/10.21105/joss.00538. https://doi.org/10.21105/joss.00538.

Ransom, Scott. 2011. *PRESTO: PulsaR Exploration and Search TOolkit.* Astrophysics Source Code Library, record ascl:1107.017, July. ascl: 1107.017.

Ransom, Scott Mitchell. 2001. New search techniques for binary pulsars. PhD diss., Harvard University, January.

Riseley, C. J., T. J. Galvin, C. Sobey, T. Vernstrom, S. V. White, X. Zhang, B. M. Gaensler et al. 2020. The POlarised GLEAM Survey (POGS) II: Results from an all-sky rotation measure synthesis survey at long wavelengths. PASA 37 (July): e029. https://doi.org/10.1017/pasa.2020.20. arXiv: 2005.09266 [astro-ph.GA].

Sanidas, S., S. Cooper, C. G. Bassa, J. W. T. Hessels, V. I. Kondratiev, D. Michilli, B. W. Stappers et al. 2019. The LOFAR Tied-Array All-Sky Survey (LOTAAS): Survey overview and initial pulsar discoveries. A&A 626 (June): A104. https://doi.org/10.1051/0004-6361/201935609. arXiv: 1905.04977 [astro-ph.HE].

Shannon, Ryan M., N. D. Ramesh Bhat, Aurelien Chalueau, Siyuan Chen, H. Thankful Cromartie, A. Gopukumar, Kathrin Grunthal et al. 2025. The SKAO Pulsar Timing Array. *The Open Journal of Astrophysics* 8 (December): 54243. https://doi.org/10.33232/001c.154243. arXiv: 2512.16163 [astro-ph.HE].

Stovall, K., P. S. Ray, J. Blythe, J. Dowell, T. Eftekhari, A. Garcia, T. J. W. Lazio, M. McCrackan, F. K. Schinzel and G. B. Taylor. 2015. Pulsar Observations Using the First Station of the Long Wavelength Array and the LWA Pulsar Data Archive. ApJ 808, no. 2 (August): 156. https://doi.org/10.1088/0004-637X/808/2/156. arXiv: 1410.7422 [astro-ph.IM].

Susarla, S. C., O. A. Johnson, D. J. McKenna, E. F. Keane, P. J. McCauley, J. P. W. Verbiest, C. Tiburzi and A. Golden. 2025. Long-term timing results of ecliptic pulsars observed with I-LOFAR. A&A 698 (June): A248. https://doi.org/10.1051/0004-6361/202554226. arXiv: 2505.09549 [astro-ph.HE].

Swainston, N. A., N. D. R. Bhat, I. S. Morrison, S. J. McSweeney, S. M. Ord, S. E. Tremblay and M. Sokolowski. 2022. MWA tied-array processing IV: A multi-pixel beamformer for pulsar surveys and ionospheric corrected localisation. PASA 39 (May): e020. https://doi.org/10.1017/pasa.2022.14. arXiv: 2203.13986 [astro-ph.IM].

Swainston, N. A., N. D. R. Bhat, M. Sokolowski, S. J. McSweeney, S. Kudale, S. Dai, K. R. Smith et al. 2021. Discovery of a Steep-spectrum Low-luminosity Pulsar with the Murchison Widefield Array. ApJ 911, no. 2 (April): L26. https://doi.org/10.3847/2041-8213/abec7b. arXiv: 2104.10018 [astro-ph.HE].

Swainston, N. A., C. P. Lee, S. J. McSweeney and N. D. R. Bhat. 2022. pulsar_spectra: A pulsar flux density catalogue and spectrum fitting repository. PASA 39 (November): e056. https://doi.org/10.1017/pasa.2022.52. arXiv: 2209.13324 [astro-ph.HE].

Tingay, S. J., R. Goeke, J. D. Bowman, D. Emrich, S. M. Ord, D. A. Mitchell, M. F. Morales et al. 2013. The Murchison Widefield Array: The Square Kilometre Array Precursor at Low Radio Frequencies. PASA 30 (January): e007. https://doi.org/10.1017/pasa.2012.007. arXiv: 1206.6945 [astro-ph.IM].

Tremblay, S. E., S. M. Ord, N. D. R. Bhat, S. J. Tingay, B. Crosse, D. Pallot, S. I. Oronsaye et al. 2015. The High Time and Frequency Resolution Capabilities of the Murchison Widefield Array. PASA 32 (February): e005. https://doi.org/10.1017/pasa.2015.6. arXiv: 1501.05723 [astro-ph.IM].

Tyul'bashev, Sergei A., Marina A. Kitaeva and Gayane E. Tyul'basheva. 2022. Pushchino multibeam pulsar search - I. Targeted search of weak pulsars. MNRAS 517, no. 1 (November): 1112–1125. https://doi.org/10.1093/mnras/stac2404. arXiv: 2203.15540 [astro-ph.HE].

van Straten, W. and M. Bailes. 2010. *DSPSR: Digital Signal Processing Software for Pulsar Astronomy.* Astrophysics Source Code Library, record ascl:1010.006, October. ascl: 1010.006.

———. 2011. DSPSR: Digital Signal Processing Software for Pulsar Astronomy. PASA 28, no. 1 (January): 1–14. https://doi.org/10.1071/AS10021. arXiv: 1008.3973 [astro-ph.IM].

van Straten, Willem, Paul Demorest, Jonathan Khoo, Mike Keith, Aidan Hotan and et al. 2011. *PSRCHIVE: Development Library for the Analysis of Pulsar Astronomical Data.* Astrophysics Source Code Library, record ascl:1105.014, May. ascl: 1105.014.

Virtanen, Pauli, Ralf Gommers, Travis E. Oliphant, Matt Haberland, Tyler Reddy, David Cournapeau, Evgeni Burovski et al. 2020. SciPy 1.0: Fundamental Algorithms for Scientific Computing in Python. *Nature Methods* 17:261–272. https://doi.org/10.1038/s41592-019-0686-2.

Wayth, Randall, Marcin Sokolowski, Jess Broderick, Steven J. Tingay, Raunaq Bhushan, Tom Booler, Riccardo Chiello et al. 2022. Engineering Development Array 2: design, performance, and lessons from an SKA-Low prototype station. *Journal of Astronomical Telescopes, Instruments, and Systems* 8 (January): 011010. https://doi.org/10.1117/1.JATIS.8.1.011010. arXiv: 2112.00908 [astro-ph.IM].

Wayth, Randall B., Steven J. Tingay, Cathryn M. Trott, David Emrich, Melanie Johnston-Hollitt, Ben McKinley, B. M. Gaensler et al. 2018. The Phase II Murchison Widefield Array: Design overview. PASA 35 (November): 33. https://doi.org/10.1017/pasa.2018.37. arXiv: 1809.06466 [astro-ph.IM].

Xue, Mengyao, N. D. R. Bhat, S. E. Tremblay, S. M. Ord, C. Sobey, N. A. Swainston, D. L. Kaplan, Simon Johnston, B. W. Meyers and S. J. McSweeney. 2017. A Census of Southern Pulsars at 185 MHz. PASA 34 (December): e070. https://doi.org/10.1017/pasa.2017.66. arXiv: 1711.08933 [astro-ph.HE].

Yao, J. M., R. N. Manchester and N. Wang. 2017. A New Electron-density Model for Estimation of Pulsar and FRB Distances. ApJ 835, no. 1 (January): 29. https://doi.org/10.3847/1538-4357/835/1/29. arXiv: 1610.09448 [astro-ph.GA].

Young, Olivia and Michael T. Lam. 2024. Redeveloping a CLEAN Deconvolution Algorithm for Scatter-broadened Radio Pulsar Signals. ApJ 962, no. 2 (February): 131. https://doi.org/10.3847/1538-4357/ad1ce7. arXiv: 2306.06046 [astro-ph.HE].

Table 2. List of all 71 SMART observations. From left to right, the columns are: the SMART pointing name, the right ascension and declination of the pointing centre, the UTC date of the observation epoch, the MWA observation IDs of the VCS and calibration observations, and the number of non-flagged tiles. The label ID (Name) corresponds to the Blue, Red, Green, Purple and Orange pointings (see Figure 1), and SCP denotes the pointing towards the South Celestial Pole.

Name	RA	Dec	UTC Date	VCS Obs ID	Cal Obs ID	#Tiles
B01	$22^h00^m13^s$	−55°06′05″	2018-09-19	1221399680	1221405408	124
B02	$22^h30^m15^s$	+01°30′28″	2018-09-24	1221832280	1221831856	126
B03	$22^h29^m41^s$	−26°47′58″	2018-10-01	1222435400	1222435120	126
B04	$23^h34^m40^s$	−13°05′29″	2018-10-04	1222697776	1222695592	125
B05	$23^h35^m29^s$	+18°32′08″	2018-10-08	1223042480	1223038272	125
B06	$23^h35^m19^s$	−40°31′14″	2018-11-08	1225713560	1225710744	124
B07	$00^h41^m18^s$	−26°48′15″	2018-11-12	1226062160	1226055688	123
B08	$00^h41^m01^s$	+01°29′50″	2019-10-18	1255444104	1255443816	124
B09	$00^h41^m44^s$	−55°06′46″	2018-10-22	1224252736	1224277624	116
B10	$00^h41^m40^s$	−72°08′41″	2018-11-23	1227009976	1227006584	126
B11	$01^h47^m29^s$	−40°30′41″	2018-10-29	1224859816	1224874512	123
B12	$01^h46^m07^s$	+18°32′49″	2018-11-01	1225118240	1225106088	123
B13	$01^h46^m53^s$	−13°04′47″	2018-11-05	1225462936	1225450648	123
R01	$02^h52^m39^s$	+01°31′31″	2019-09-10	1252177744	1252187184	77
R02	$02^h52^m43^s$	−26°47′07″	2019-09-17	1252780888	1252780600	123
R03	$03^h22^m19^s$	−55°05′06″	2019-09-25	1253471952	1253482168	124
R04	$03^h58^m31^s$	−40°28′41″	2019-10-01	1253991112	1253990824	122
R05	$03^h58^m07^s$	+18°35′07″	2019-10-08	1254594264	1254599656	124
R06	$03^h58^m15^s$	−13°02′39″	2019-10-15	1255197408	1255202808	116
R07	$04^h43^m02^s$	−72°05′12″	2019-10-22	1255803168	1255813280	122
R08	$05^h03^m47^s$	+01°34′42″	2019-10-29	1256407632	1256417736	123
R09	$05^h04^m03^s$	−26°43′54″	2019-11-05	1257010784	1257010488	119
R10	$06^h02^m48^s$	−55°00′51″	2019-11-12	1257617424	1257626800	124
R11	$06^h09^m50^s$	−40°25′02″	2019-11-19	1258221008	1258226400	124
R12	$06^h09^m13^s$	+18°38′45″	2019-12-06	1259685792	1259691192	112
R13	$06^h09^m33^s$	−12°58′59″	2019-12-03	1259427304	1259427008	113
G01	$07^h24^m57^s$	+01°38′45″	2019-12-17	1260638120	1260637840	114
G02	$07^h25^m13^s$	−26°39′49″	2019-12-24	1261241272	1261240560	112
G03	$08^h20^m55^s$	−40°21′11″	2020-02-17	1265983624	1265983344	116
G04	$08^h20^m26^s$	+18°42′20″	2020-02-14	1265725128	1265724848	122
G05	$08^h20^m41^s$	−12°55′15″	2020-02-19	1266155952	1266155672	117
G06	$08^h43^m08^s$	−54°56′15″	2020-02-21	1266329600	1266329312	125
G07	$08^h43^m34^s$	−71°58′20″	2020-02-28	1266932744	1266938144	125
G08	$09^h26^m12^s$	+01°41′38″	2020-02-04	1264867416	1264850632	105
G09	$09^h26^m24^s$	−26°36′55″	2020-02-11	1265470568	1265475968	124
G10	$10^h31^m53^s$	−40°18′57″	2020-02-25	1266680784	1266686192	124
G11	$10^h31^m45^s$	+18°44′42″	2020-03-01	1267111608	1267111328	124
G12	$10^h31^m51^s$	−12°52′57″	2020-03-03	1267283936	1267289336	122
G13	$11^h23^m06^s$	−54°54′09″	2020-03-05	1267459328	1267459048	124
G14	$11^h37^m22^s$	+01°43′04″	2020-03-12	1268063336	1268063056	124
G15	$11^h37^m27^s$	−26°35′29″	2020-03-15	1268321832	1268327232	124
P01	$12^h39^m18^s$	−12°52′13″	2021-03-26	1300809400	1300814800	119
P02	$12^h39^m20^s$	+18°45′27″	2021-03-28	1300981728	1300981448	118
P03	$12^h39^m06^s$	−71°55′55″	2021-03-31	1301240224	1301239936	118
P04	$12^h39^m18^s$	−40°18′11″	2021-04-02	1301412552	1301412264	118
P05	$13^h44^m51^s$	−26°35′50″	2021-04-05	1301674968	1301674688	119
P06	$13^h44^m57^s$	+01°42′45″	2021-04-07	1301847296	1301847016	118
P07	$13^h58^m58^s$	−54°54′37″	2021-04-10	1302106648	1302106368	118
P08	$14^h50^m30^s$	−12°53′58″	2021-04-17	1302712864	1302712576	118
P09	$14^h50^m41^s$	+18°43′45″	2021-04-15	1302540536	1302540248	120
P10	$14^h50^m15^s$	−40°19′59″	2021-04-12	1302282040	1302281760	113
P11	$15^h55^m45^s$	−26°38′02″	2023-06-18	1371131072	1371130952	140
P12	$15^h56^m04^s$	+01°40′30″	2023-05-07	1367512184	1367512064	125
P13	$16^h38^m07^s$	−72°00′10″	2023-05-05	1367342464	1367342344	129
P14	$16^h39^m00^s$	−54°58′02″	2023-05-06	1367428632	1367428512	126
O01	$17^h01^m30^s$	−12°57′08″	2023-05-12	1367946928	1367946808	122
O02	$17^h01^m51^s$	+18°40′36″	2023-05-13	1368033096	1368032976	123
O03	$17^h01^m15^s$	−40°23′08″	2023-05-19	1368550080	1368549960	126

Continued on next page

https://doi.org/10.1017/pasa.2026.10229

Continued from previous page

Name	RA	Dec	UTC Date	VCS Obs ID	Cal Obs ID	#Tiles
O04	$18^h07^m00^s$	$-26°42'22''$	2023-05-20	1368640168	1368640048	124
O05	$18^h07^m19^s$	$+01°36'15''$	2023-05-29	1369415648	1369415528	122
O06	$19^h12^m46^s$	$-13°01'34''$	2023-05-30	1369505736	1369510536	129
O07	$19^h12^m59^s$	$+18°36'12''$	2023-06-02	1369764224	1369769024	137
O08	$19^h12^m23^s$	$-40°27'36''$	2023-06-04	1369936552	1369941352	137
O09	$19^h19^m22^s$	$-55°03'26''$	2023-06-09	1370367808	1370372608	123
O10	$20^h18^m14^s$	$-26°46'37''$	2023-06-10	1370457464	1370457344	129
O11	$20^h18^m24^s$	$+01°31'56''$	2023-07-14	1373387040	1373386920	133
O12	$20^h39^m09^s$	$-72°07'59''$	2023-06-19	1371234256	1371234136	140
O13	$21^h23^m56^s$	$-13°05'17''$	2023-06-23	1371581520	1371581400	133
O14	$21^h24^m10^s$	$+18°32'29''$	2023-07-02	1372357000	1372361800	139
O15	$21^h23^m46^s$	$-40°31'20''$	2023-06-30	1372184672	1372184552	130
SCP	$05^h32^m49^s$	$-82°48'46''$	2023-11-14	1384018160	1384018040	117

https://doi.org/10.1017/pasa.2026.10229

Table 3. Summary of the 205 non-recycled pulsars re-detected in SMART observations. For each pulsar, we list the J-name, the B-name (where available), the Galactic longitude and latitude (l, b), the spin period, and the DM from `pdmp`. For the best detection of each pulsar, we list the S/N reported by PSRCHIVE, the mean and peak flux densities at 154 MHz ($S_{\rm mean}$ and $S_{\rm p}$), the observed RM and the estimated (ionosphere-corrected) RM from the IISM, the estimated pulse widths at 10% and 50% of the peak flux density, the SMART pointing label (see Table 2), the integration time ($T_{\rm obs}$), and the mean offset from the pointing centre. Notes: † More precise than the measurement in the ATNF pulsar catalogue (v2.7.0). †† No previous RM measurement available in the ATNF pulsar catalogue (v2.7.0). ‡ Main and interpulse measurements. ‡‡ Since the main and interpulse overlap for the Crab pulsar, the W_{10} is made across both pulses.

PSR J	PSR B	l [°]	b [°]	Period [ms]	DM [cm^{-3} pc]	S/N	$S_{\rm mean}$ [mJy]	$S_{\rm p}$ [Jy]	RM$_{\rm obs}$ [rad m^{-2}]	RM$_{\rm IISM}$ [rad m^{-2}]	W_{10} [ms]	W_{50} [ms]	Pointing label	$T_{\rm obs}$ [min]	Offset [°]
J0026–1955	–	83.3	–80.8	1306.15	20.74(11)	44.8	49(15)	0.86(26)	3.57(10)	4.40(15)††	128.4	82.2	B07	80	9.0
J0034–0721	B0031–07	110.4	–69.8	942.95	10.88(8)	801.7	$8.5(2.5)\times10^{2}$	11.1(3.3)	9.797(8)	10.63(11)	129.6	69.4	B04	43	11.7
J0036–1033	–	110.0	–73.0	900.01	23.14(8)	11.6	26(9)	0.91(28)	–8.22(11)	–7.41(15)†	38.1	22.7	B04	43	10.9
J0038–2501	–	67.4	–86.4	256.93	5.675(22)	98.4	61(18)	1.8(6)	7.37(23)	8.16(26)††	16.8	8.5	B07	80	5.0
J0133–6957	–	297.7	–46.7	463.47	22.92(4)	9.6	18(6)	0.70(22)	24.94(32)	25.40(32)†	17.8	11.6	B09	54	15.6
J0134–2937	–	230.3	–80.2	136.96	21.818(24)	8.6	14(5)	0.22(8)	–	–	–	11.6	B07	61	10.1
J0151–0635	B0148–06	160.4	–65.0	1464.66	25.83(12)	67.3	64(19)	1.8(6)	–6.74(5)	–5.64(13)	199.4	170.7	B13	80	8.5
J0152–1637	B0149–16	179.3	–72.5	832.74	11.92(7)	173.5	$1.2(4)\times10^{2}$	6.5(2.0)	6.48(8)	7.35(13)†	31.9	8.3	B07	28	14.6
J0206–4028	B0203–40	258.6	–69.6	630.55	12.97(5)	275.2	$1.9(6)\times10^{2}$	13(4)	2.869(32)	3.38(8)†	14.6	7.5	B11	30	1.4
J0255–5304	B0254–53	269.9	–55.3	447.71	17.98(4)	33.3	55(17)	2.3(7)	27.04(5)	27.60(12)†	21.2	11.6	R03	60	5.8
J0401–7608	B0403–76	290.3	–35.9	545.25	21.96(5)	60.1	93(28)	7.4(2.2)	23.28(10)	23.69(12)	17.6	4.4	R07	30	4.2
J0418–4154	–	246.3	–45.7	757.12	24.29(6)	142.8	89(27)	4.1(1.2)	21.287(34)	21.81(14)††	28.8	13.5	R04	47	2.8
J0450–1248	B0447–12	211.1	–32.6	438.01	37.02(4)	167.1	$2.0(6)\times10^{2}$	8.3(2.5)	7.24(11)	7.87(20)	22.0	7.4	R06	17	5.0
J0452–1759	B0450–18	217.1	–34.1	548.94	39.90(5)	466.6	$6.0(1.8)\times10^{2}$	12(4)	12.473(5)	13.08(16)	45.5	32.1	R06	17	7.5
J0514–4408	–	249.5	–35.4	320.27	15.207(27)	28.7	76(23)	0.81(25)	17.26(9)	17.76(16)†	40.0,26.7‡	18.7,4.6‡	R04	47	11.7
J0520–2553	–	228.4	–30.5	241.64	33.790(21)	9.3	16(6)	1.16(35)	–	–	11.0	2.7	R11	30	15.5
J0525+1115	B0523+11	192.7	–13.2	354.44	79.398(30)	29.4	84(26)	1.2(4)	–	–	55.6	22.4	R12	50	10.4
J0528+2200	B0525+21	183.9	–6.9	3745.54	50.69(32)	151.9	$1.2(5)\times10^{2}$	6.0(2.4)	–39.769(26)	–38.86(18)	252.4	210.8	R12	50	7.1
J0534+2200	B0531+21	184.6	–5.8	33.39	56.7600(29)	470.4	$7.1(2.8)\times10^{3}$	25(10)	–47.538(4)	–46.63(17)	23.9‡‡	5.6	R12	20	10.4
J0536–7543	B0538–75	287.2	–30.8	1245.86	18.13(12)	31.1	58(18)	1.3(4)	26.52(16)	26.93(17)	153.4	68.3	G07	34	11.7
J0600–5756	B0559–57	266.5	–29.3	2261.36	21.54(19)	90.3	58(18)	2.2(7)	29.90(4)	30.32(10)††	94.7	53.0	R10	80	4.2
J0614+2229	B0611+22	188.8	2.4	334.96	96.975(29)	54.6	$1.2(5)\times10^{2}$	1.9(7)	67.022(33)	67.94(17)†	48.3	11.9	R12	80	6.4
J0630–2834	B0628–28	237.0	–16.8	1244.43	34.44(11)	836.8	$8.8(2.6)\times10^{2}$	14(4)	45.653(6)	46.28(11)	128.6	69.7	R11	30	12.4
J0636–4549	–	254.5	–21.5	1984.60	25.88(17)	11.4	33(12)	2.5(7)	–	–	59.5	23.8	R11	10	9.3
J0702–4956	–	260.2	–18.7	665.99	98.73(20)	9.2	28(10)	0.44(16)	–	–	–	56.4	G06	37	12.9
J0725–1635	–	231.5	–0.3	424.31	99.08(5)	7.7	22(10)	0.44(19)	–	–	–	22.5	G05	30	8.3
J0726–2612	–	240.1	–4.6	3442.31	69.74(29)	7.7	20(10)	0.58(25)	–	–	–	104.6	G02	30	1.8
J0729–1448	–	230.4	1.4	251.71	91.920(21)	19.2	55(23)	1.2(5)	46.69(7)	47.42(14)	21.0	10.2	G05	30	6.7
J0729–1836	B0727–18	233.8	–0.3	510.18	61.34(6)	17.8	47(20)	0.9(4)	–	–	–	34.4	G02	30	8.3
J0742–2822	B0740–28	243.8	–2.4	166.76	73.818(14)	355.3	$6.6(2.6)\times10^{2}$	4.9(2.0)	149.835(9)	150.57(10)	48.7	17.4	G02	80	5.8
J0746–4529	–	259.2	–10.1	2791.03	134.4(4)	8.3	17(7)	0.43(14)	–	–	–	131.4	G06	68	12.6
J0750–6846	–	281.1	–20.0	915.22	54.27(8)	8.2	12(5)	0.44(14)	–	–	–	30.0	G07	80	5.6
J0758–1528	B0756–15	234.5	7.2	682.27	63.33(6)	23.6	43(18)	2.8(1.1)	48.89(20)	49.61(24)	17.2	8.9	G05	30	3.2
J0820–1350	B0818–13	235.9	12.6	1238.13	40.88(11)	1129.4	$6.3(1.9)\times10^{2}$	37(11)	–2.945(19)	–2.21(14)	38.1	19.7	G05	30	2.1
J0820–3921	–	257.3	–1.6	1073.57	181.3(8)	9.8	38(16)	0.34(16)	–	–	–	–	G02	30	14.3
J0820–4114	B0818–41	258.7	–2.7	545.45	113.36(5)	79.8	$2.0(8)\times10^{2}$	1.1(5)	60.76(28)	61.29(30)	305.6	60.3	G06	80	14.7
J0823+0159	B0820+02	222.0	21.2	864.87	23.72(7)	32.3	63(19)	1.7(5)	17.34(22)	18.19(27)†	56.0	35.3	G05	30	15.1
J0835–4510	B0833–45	263.6	–2.8	89.33	67.834(8)	311.5	$6.2(2.5)\times10^{3}$	14(6)	43.934(5)	44.45(10)	72.6	35.1	G06	80	10.5
J0837+0610	B0834+06	219.7	26.3	1273.77	12.88(11)	1820.1	$5.8(1.7)\times10^{2}$	33(10)	25.574(11)	26.33(15)	37.1	24.1	G08	30	7.6
J0837–4135	B0835–41	260.9	–0.3	751.63	147.25(6)	195.0	$2.0(8)\times10^{2}$	5.7(2.3)	146.23(12)	146.76(16)	50.8	19.4	G06	80	13.9
J0842–4851	B0840–48	267.2	–4.1	644.37	196.85(10)	51.8	$1.5(6)\times10^{2}$	0.75(31)	–	–	411.4	91.4	G06	80	7.0
J0849–6322	–	279.4	–12.2	367.95	91.350(31)	13.1	27(9)	0.63(20)	–91.96(21)	–91.42(23)†	26.3	10.2	G07	80	8.9

Continued on next page

Continued from previous page

PSR J	PSR B	l [°]	b [°]	Period [ms]	DM [$\mathrm{cm^{-3}\,pc}$]	S/N	S_{mean} [mJy]	S_{p} [Jy]	$\mathrm{RM_{obs}}$ [$\mathrm{rad\,m^{-2}}$]	$\mathrm{RM_{IISM}}$ [$\mathrm{rad\,m^{-2}}$]	W_{10} [ms]	W_{50} [ms]	Pointing label	T_{obs} [min]	Offset [°]
J0855–3331	B0853–33	256.8	7.5	1267.54	86.72(11)	46.2	9(4)e+01	1.2(5)	148.91(27)	149.48(30)	241.6	52.5	G09	60	8.8
J0856–6137	B0855–61	278.6	–10.4	962.51	95.76(8)	251.2	$1.9(6)\times10^2$	7.2(2.2)	–114.65(7)	–114.23(11)†	43.6	22.8	G06	80	7.5
J0902–6325	B0901–63	280.4	–11.1	660.31	72.85(6)	35.7	45(14)	2.9(9)	–53.62(7)	–53.08(11)	24.1	5.0	G07	80	9.0
J0904–4246	B0903–42	265.1	2.9	965.17	146.4(4)	16.0	37(15)	0.29(13)	–	–	–	166.3	G06	80	13.2
J0904–7459	B0904–74	289.7	–18.3	549.55	49.26(6)	21.2	33(10)	0.59(18)	6.56(22)	7.00(23)	56.2	35.0	G07	80	3.7
J0905–6019	–	278.2	–8.8	340.85	91.635(29)	48.6	56(23)	2.1(8)	–67.27(16)	–66.84(18)†	17.1	7.9	G06	80	6.8
J0907–5157	B0905–51	272.2	–3.0	253.56	103.80(5)	78.0	$2.2(9)\times10^2$	0.82(33)	–25.57(14)	–25.09(17)	156.6	61.7	G06	80	5.4
J0908–1739	B0906–17	246.1	19.8	401.63	15.854(34)	131.3	105(32)	4.2(1.3)	–34.98(7)	–34.34(15)†	24.2	7.5	G09	60	9.9
J0922+0638	B0919+06	225.4	36.4	430.63	27.28(4)	221.0	$2.0(6)\times10^2$	6.2(1.8)	–	–	30.2	10.4	G08	30	8.8
J0924–5302	B0922–52	274.7	–1.9	746.34	153.47(6)	335.5	$3.0(1.2)\times10^2$	8.0(3.2)	116.39(8)	116.87(12)	54.9	20.2	G06	80	6.5
J0924–5814	B0923–58	278.4	–5.6	739.51	57.40(6)	68.0	$1.0(4)\times10^2$	1.5(6)	–45.209(32)	–44.77(9)	86.9	46.2	G06	80	6.9
J0934–5249	B0932–52	275.7	–0.7	1444.78	100.26(12)	58.4	$1.1(4)\times10^2$	3.8(1.5)	10.19(15)	10.67(17)	72.0	29.0	G06	80	8.0
J0940–5428	–	277.5	–1.3	87.57	134.88(10)	15.7	53(22)	0.32(14)	–	–	–	36.3	G06	80	8.4
J0941–5244	–	276.4	0.1	658.56	158.27(6)	14.8	37(15)	0.76(31)	–193.5(5)	–193.1(5)	59.4	28.4	G06	80	9.0
J0942–5552	B0940–55	278.6	–2.2	664.39	180.09(6)	71.3	9(4)e+01	2.2(9)	–	–	48.0	19.5	G07	60	17.0
J0942–5657	B0941–56	279.3	–3.0	808.17	160.23(7)	338.7	$2.6(1.0)\times10^2$	13(5)	141.808(14)	142.26(9)†	27.7	12.9	G06	80	8.7
J0943+1631	B0940+16	216.6	45.4	1087.42	19.71(34)	8.2	24(8)	0.27(10)	–	–	–	110.7	G08	30	15.0
J0944–1354	B0942–13	249.1	28.8	570.26	12.49(5)	12.5	21(7)	1.3(4)	–12.26(19)	–11.57(23)	18.1	7.4	G12	30	9.8
J0946+0951	B0943+10	225.4	43.1	1097.71	15.27(9)	23.0	48(15)	1.3(4)	–	–	72.8	34.8	G11	30	12.6
J0949–6902	–	287.8	–11.7	640.02	93.16(5)	56.1	50(15)	2.5(8)	–	–	26.6	7.6	G07	80	6.3
J0953+0755	B0950+08	228.9	43.7	253.07	2.979(22)	442.9	$5.6(1.7)\times10^2$	10.1(3.0)	0.976(11)	2.04(14)	23.2	11.7	G11	30	13.1
J0955–5304	B0953–52	278.3	1.2	862.12	156.78(7)	41.1	78(31)	2.8(1.1)	–130.12(19)	–129.65(21)	48.1	17.1	G06	72	10.2
J0959–4809	B0957–47	275.7	5.4	670.09	92.42(6)	54.6	$1.0(4)\times10^2$	2.0(8)	39.42(8)	39.88(12)	135.2	112.8	G10	63	9.8
J1001–5507	B0959–54	280.2	0.1	1436.64	130.20(19)	65.7	$1.7(7)\times10^2$	1.0(4)	–	–	735.7	222.0	G06	69	10.5
J1001–5559	–	280.7	–0.6	1661.18	158.9(4)	10.3	21(9)	0.34(15)	–	–	–	119.8	G07	42	17.2
J1003–4747	B1001–47	276.0	6.1	307.07	98.50(4)	8.6	19(8)	0.44(18)	–	–	–	21.6	G10	63	9.2
J1006–6311	–	285.6	–6.0	835.80	196.28(11)	11.9	22(9)	0.34(14)	–	–	–	43.4	G07	80	11.8
J1012–2337	B1010–23	262.1	26.4	2517.95	22.39(21)	23.1	55(17)	1.9(6)	56.41(13)	57.04(17)†	103.0	69.1	G12	30	11.3
J1016–5345	B1014–53	281.2	2.5	769.59	67.20(7)	5.9	19(10)	0.9(4)	–	–	–	26.5	G06	30	10.0
J1018–1642	B1016–16	258.3	32.6	1804.70	48.91(15)	13.3	32(10)	1.6(5)	–40.93(10)	–40.25(15)†	68.9	39.5	G12	30	4.5
J1020–5921	–	284.7	–1.9	1238.31	79.58(11)	11.3	35(15)	0.9(4)	–	–	59.3	23.3	G06	54	12.3
J1041–1942	B1039–19	265.6	33.6	1386.37	33.71(4)	99.6	62(19)	2.6(8)	–28.43(6)	–27.75(13)	87.5	75.8	G12	80	8.9
J1055–6905	–	292.9	–8.5	2919.40	142.57(26)	12.7	7(4)	0.33(14)	–	–	–	123.0	G07	62	10.6
J1057–5226	B1055–52	286.0	6.6	197.12	29.720(17)	146.7	$7.0(2.8)\times10^2$	6.3(2.5)	46.223(11)	46.73(10)	16.3,27.2‡	12.7,9.3‡	G13	54	3.8
J1057–7914	B1056–78	297.6	–17.6	1347.40	51.76(11)	7.3	16(6)	0.69(21)	–18.17(28)	–17.78(29)	57.9	28.7	G07	80	10.8
J1059–5742	B1056–57	288.3	1.9	1185.00	108.89(10)	65.1	$1.3(5)\times10^2$	2.8(1.1)	–57.58(21)	–57.10(23)	105.7	42.2	G13	54	3.9
J1112–6926	B1110–69	294.4	–8.2	820.49	148.55(7)	12.6	31(13)	1.1(4)	–53.0(6)	–52.5(6)	55.5	21.6	G07	46	11.1
J1116–4122	B1114–41	284.5	18.1	943.17	40.59(8)	385.8	$2.3(7)\times10^2$	11.4(3.4)	–23.97(7)	–23.47(12)	26.1	16.5	G10	63	9.2
J1121–5444	B1119–54	290.1	5.9	535.79	205.10(30)	20.3	$1.2(5)\times10^2$	0.76(33)	–	–	–	130.7	P03	30	18.1
J1123–4844	–	288.3	11.6	244.84	93.585(21)	9.5	17(6)	0.59(19)	–	–	–	19.2	G10	59	12.7
J1123–6651	–	294.5	–5.4	232.98	111.316(30)	14.8	53(22)	0.69(29)	–	–	–	20.6	G07	23	12.5
J1136+1551	B1133+16	241.9	69.2	1187.92	4.73(10)	504.2	$4.8(1.4)\times10^2$	21(6)	3.569(11)	4.75(8)	48.0	38.7	P02	33	9.9
J1136–5525	B1133–55	292.3	5.9	364.71	85.214(31)	22.1	86(35)	1.3(5)	31.12(18)	31.73(19)	44.8	20.4	P03	50	17.3
J1141–6545	–	295.8	–3.9	393.90	116.240(34)	20.2	68(28)	1.5(6)	–88.31(15)	–87.80(16)†	33.9	15.9	P03	80	8.2
J1146–6030	B1143–60	295.0	1.3	273.37	111.75(4)	13.4	34(15)	0.49(21)	4.28(19)	4.84(19)	–	26.8	P03	80	12.7
J1202–5820	B1159–58	296.5	3.9	452.80	145.94(9)	14.1	9(4)e+01	0.8(4)	–	–	–	50.5	P07	30	13.0
J1224–6407	B1221–63	300.0	–1.4	216.48	97.787(18)	13.5	9(4)e+01	1.8(7)	–3.04(32)	–2.60(32)	–	9.9	P07	30	12.7
J1225–5556	–	299.3	6.7	1018.45	125.77(10)	5.7	34(18)	0.9(4)	–	–	–	43.0	P07	30	9.7

Continued on next page

Continued from previous page

PSR J	PSR B	l [°]	b [°]	Period [ms]	DM [cm^{-3} pc]	S/N	S_{mean} [mJy]	S_{p} [Jy]	$\mathrm{RM}_{\mathrm{obs}}$ [rad m^{-2}]	$\mathrm{RM}_{\mathrm{IISM}}$ [rad m^{-2}]	W_{10} [ms]	W_{50} [ms]	Pointing label	T_{obs} [min]	Offset [°]
J1238+2152	–	272.8	84.0	1118.59	17.92(10)	13.1	23(7)	1.6(5)	3.97(19)	5.21(21)	34.6	10.2	P02	80	5.9
J1239+2453	B1237+25	252.5	86.5	1382.45	9.19(12)	76.1	71(22)	5.2(1.6)	–0.81(4)	0.47(9)	66.3	8.1	P02	80	8.0
J1239–6832	B1236–68	301.9	–5.7	1301.92	93.81(11)	4.8	23(15)	1.2(5)	–	–	–	–	P07	30	15.0
J1240–4124	B1237–41	300.7	21.4	512.24	43.29(4)	57.5	77(24)	5.4(1.6)	28.79(15)	29.48(15)†	12.5	5.1	P04	80	4.0
J1257–1027	B1254–10	305.2	52.4	617.31	29.68(5)	10.5	29(10)	1.4(4)	–0.68(26)	0.23(26)	31.2	23.4	P01	30	6.9
J1311–1228	B1309–12	310.7	50.1	447.52	36.19(4)	36.5	69(21)	3.7(1.1)	–12.73(9)	–11.84(11)†	15.0	6.3	P01	30	10.0
J1312–5402	B1309–53	306.0	8.7	728.15	135.40(19)	12.4	9(4)e+01	1.3(5)	–	–	–	58.5	P07	30	3.3
J1313+0931	–	320.4	71.7	848.93	12.00(7)	10.7	27(10)	1.9(6)	2.08(15)	2.96(17)	31.4	15.0	P06	30	8.8
J1320–5359	B1317–53	307.3	8.6	279.74	97.350(24)	26.2	$1.6(7)\times10^{2}$	3.4(1.4)	147.96(18)	148.48(19)	26.0	11.5	P07	30	2.2
J1328–4357	B1325–43	309.9	18.4	532.70	41.28(5)	14.2	76(26)	3.1(9)	–34.64(17)	–34.06(18)	30.4	20.8	P07	30	11.1
J1335–3642	–	312.7	25.3	399.19	41.805(34)	34.2	70(22)	1.9(6)	–16.31(15)	–15.57(15)†	41.0	31.7	P04	60	9.9
J1340–6456	B1336–64	308.0	–2.6	378.63	76.745(32)	8.3	52(24)	1.8(7)	–	–	–	16.2	P07	30	10.1
J1355–5153	B1352–51	313.0	9.7	644.30	111.50(5)	147.1	$4.3(1.7)\times10^{2}$	18(7)	–73.47(14)	–72.94(15)†	30.2	9.9	P07	30	3.3
J1401–6357	B1358–63	310.6	–2.1	842.81	97.81(7)	10.2	43(22)	2.6(1.0)	54.94(21)	55.40(21)	–	20.9	P07	30	9.5
J1418–3921	–	320.8	20.5	1096.81	60.16(9)	32.5	$1.7(5)\times10^{2}$	5.0(1.5)	–	–	60.4	24.2	P07	30	15.6
J1428–5530	B1424–55	316.4	4.8	570.29	82.04(5)	20.5	$1.4(6)\times10^{2}$	2.3(1.0)	–4.15(18)	–3.63(18)	54.2	30.0	P07	30	1.4
J1430–6623	B1426–66	312.7	–5.4	785.44	65.09(7)	79.8	$2.4(1.0)\times10^{2}$	15(6)	–21.19(7)	–20.74(7)	27.4	6.0	P07	30	11.5
J1440–6344	B1436–63	314.6	–3.4	459.61	123.94(4)	11.4	56(24)	1.6(7)	–	–	40.6	12.2	P13	50	12.5
J1453–6413	B1449–64	315.7	–4.4	179.49	71.080(15)	406.7	$1.1(5)\times10^{3}$	50(20)	–21.728(10)	–21.26(4)	7.1	3.4	P07	30	10.1
J1456–6843	B1451–68	313.9	–8.5	263.38	8.620(22)	298.5	$6.6(2.7)\times10^{2}$	19(8)	–2.753(26)	–2.05(4)	36.6	5.2	P13	80	9.1
J1507–4352	B1504–43	327.3	12.5	286.76	49.170(24)	24.8	$2.0(6)\times10^{2}$	9.8(3.0)	–34.052(35)	–33.45(6)	10.0	5.2	P07	30	13.2
J1510–4422	B1507–44	327.6	11.7	943.87	84.29(8)	10.4	70(25)	2.3(7)	–	–	–	22.6	P07	30	13.0
J1514–4834	B1510–48	325.9	7.8	454.84	49.37(4)	11.9	29(14)	0.78(33)	–6.90(25)	–6.27(26)†	–	18.8	P10	60	10.5
J1527–3931	B1524–39	333.0	14.0	2417.61	48.85(21)	26.6	57(19)	3.5(1.1)	–10.93(14)	–10.24(15)†	70.2	24.8	P10	60	9.2
J1534–5334	B1530–53	325.7	1.9	1368.88	24.73(12)	200.3	$3.4(1.4)\times10^{2}$	20(8)	22.57(8)	23.50(9)	56.4	11.5	P14	80	9.5
J1543–0620	B1540–06	0.6	36.6	709.06	18.36(6)	10.3	83(27)	4.8(1.5)	–6.10(15)	–4.57(17)	21.7	8.1	O01	23	13.8
J1543+0929	B1541+09	17.8	45.8	748.45	35.05(6)	42.3	$2.1(6)\times10^{2}$	3.1(1.0)	15.71(15)	17.17(16)	85.9	43.7	O02	15	14.4
J1544–5308	B1541–52	327.3	1.3	178.55	35.036(24)	16.8	79(33)	1.5(6)	–	–	–	13.4	P14	80	8.1
J1549–4848	–	330.5	4.3	288.35	56.227(25)	8.4	39(19)	1.7(7)	–	–	–	7.2	P14	80	10.0
J1555–2341	B1552–23	348.4	22.5	532.58	51.80(7)	26.4	81(25)	0.97(31)	–	–	–	33.7	P11	74	5.4
J1555–3134	B1552–31	342.7	16.8	518.11	73.02(4)	24.8	92(28)	1.6(5)	–50.55(11)	–49.51(12)†	70.2	41.0	P11	74	6.7
J1559–4438	B1556–44	334.5	6.4	257.06	56.33(5)	10.0	67(29)	1.0(4)	–4.73(31)	–3.70(31)	–	29.0	P14	80	12.5
J1603–2712	B1600–27	347.1	18.8	778.32	46.26(7)	189.4	$3.1(9)\times10^{2}$	15(4)	–10.07(5)	–8.99(7)	30.1	12.9	P11	74	4.6
J1604–4909	B1600–49	332.2	2.4	327.42	140.70(12)	11.2	75(32)	0.8(4)	–	–	–	33.2	P14	80	8.3
J1607–0032	B1604–00	10.7	35.5	421.82	10.69(4)	18.6	90(29)	3.2(1.0)	–	–	20.9	14.0	O01	32	14.6
J1612–2408	–	351.0	19.4	923.83	49.08(8)	20.5	59(19)	2.5(8)	–39.69(25)	–38.58(25)††	33.6	21.4	P11	74	6.3
J1614+0737	B1612+07	20.6	38.2	1206.80	21.43(10)	13.3	91(29)	8.8(2.7)	–	–	26.1	8.8	O02	20	11.9
J1615–5537	B1611–55	329.0	–3.5	791.53	124.75(7)	9.6	66(28)	1.5(6)	–	–	–	29.7	P14	80	3.9
J1627+1419	–	30.0	38.3	490.86	32.15(14)	9.5	37(15)	0.69(26)	–	–	–	40.0	O02	24	11.3
J1635–5954	B1630–59	327.7	–8.3	529.12	134.08(14)	12.5	9(4)e+01	1.7(7)	–	–	–	16.0	P14	80	5.8
J1645–0317	B1642–03	14.1	26.1	387.69	35.740(33)	481.8	$5.5(1.6)\times10^{2}$	45(14)	15.409(33)	16.94(7)	7.0	3.5	O01	78	11.6
J1646–6831	B1641–68	321.8	–14.8	1785.61	42.14(15)	19.5	68(21)	3.6(1.1)	103.65(31)	104.38(31)	117.3	18.8	P13	80	4.0
J1648–3256	–	349.6	7.7	719.46	128.45(6)	10.9	48(20)	1.1(4)	–	–	–	18.9	P11	53	11.9
J1654–2713	–	355.0	10.3	791.82	92.64(7)	11.7	54(18)	1.08(35)	–	–	–	31.8	P11	48	11.0
J1703–3241	B1700–32	351.8	5.4	1211.79	110.33(18)	19.3	$1.6(7)\times10^{2}$	2.3(1.0)	–	–	–	86.9	O03	48	8.6
J1703–4851	–	339.0	–4.5	1396.40	149.3(6)	14.4	$1.0(4)\times10^{2}$	0.78(35)	–	–	–	206.3	P14	80	7.9
J1704–6016	B1659–60	329.8	–11.4	306.32	51.285(26)	25.1	$1.7(5)\times10^{2}$	2.2(7)	–	–	113.9	10.8	P14	80	6.9
J1709–1640	B1706–16	5.8	13.7	653.06	24.86(6)	172.2	$2.6(8)\times10^{2}$	12(4)	–2.220(25)	–0.85(6)	24.1	11.8	O01	80	6.6

Continued on next page

Continued from previous page

PSR J	PSR B	l [°]	b [°]	Period [ms]	DM [cm^{-3} pc]	S/N	$S_{\rm mean}$ [mJy]	$S_{\rm p}$ [Jy]	RM$_{\rm obs}$ [rad m^{-2}]	RM$_{\rm IISM}$ [rad m^{-2}]	W_{10} [ms]	W_{50} [ms]	Pointing label	$T_{\rm obs}$ [min]	Offset [°]
J1711–5350	B1707–53	335.7	–8.5	899.23	105.14(8)	13.2	9(4)e+01	3.7(1.5)	–	–	41.1	18.0	P14	80	5.2
J1720–2933	B1717–29	356.5	4.2	620.45	42.40(12)	8.1	1.1(5)$\times10^2$	1.7(8)	–	–	–	38.9	O03	20	14.8
J1722–3207	B1718–32	354.6	2.5	477.16	125.61(20)	20.9	4.2(1.7)$\times10^2$	1.5(7)	–	–	–	186.7	O03	48	8.8
J1722–3712	B1719–37	350.5	–0.5	236.18	99.52(35)	13.2	1.2(5)$\times10^2$	0.9(4)	–	–	–	–	O03	80	6.4
J1731–4744	B1727–47	342.6	–7.7	829.95	123.28(7)	197.1	5.4(2.1)$\times10^2$	15(6)	–451.96(14)	–450.96(14)	52.3	26.1	P14	79	11.2
J1735–0724	B1732–07	17.3	13.3	419.33	73.35(4)	19.2	1.6(5)$\times10^2$	2.3(7)	–	–	–	15.6	O05	30	9.4
J1740+1311	B1737+13	37.1	21.7	803.05	48.70(7)	5.7	54(18)	2.3(7)	–	–	27.6	15.9	O02	30	8.5
J1741–0840	B1738–08	17.0	11.3	2043.08	74.9(7)	8.7	46(19)	0.93(35)	–	–	–	150.9	O05	30	10.5
J1743–1351	B1740–13	12.7	8.2	405.34	116.32(6)	11.0	1.0(4)$\times10^2$	1.8(8)	–	–	–	26.6	O01	30	4.3
J1745–3040	B1742–30	358.6	–1.0	367.44	88.16(9)	20.1	1.6(7)$\times10^2$	1.4(6)	–	–	–	37.9	O04	80	7.3
J1748–1300	B1745–12	14.0	7.7	394.13	99.46(10)	9.8	1.0(4)$\times10^2$	1.4(6)	–	–	–	50.8	O01	30	5.3
J1751–4657	B1747–46	345.0	–10.2	742.35	20.55(6)	251.2	3.4(1.0)$\times10^2$	13(4)	17.203(24)	17.98(5)	26.0	19.0	O09	41	13.4
J1752–2806	B1749–28	1.5	–1.0	562.57	50.40(5)	970.7	3.6(1.4)$\times10^3$	1.7(7)e+02	94.83(9)	96.05(10)	19.5	10.2	O04	59	3.7
J1801–0357	B1758–03	23.6	9.3	921.49	120.26(17)	13.0	1.4(6)$\times10^2$	1.8(7)	–	–	–	30.2	O05	30	7.6
J1807–0847	B1804–08	20.1	5.6	163.73	112.31(21)	14.7	1.8(7)$\times10^2$	0.9(4)	–	–	–	–	O05	30	10.6
J1819–1318	–	17.5	0.8	1515.70	37.12(13)	6.6	54(29)	2.7(1.1)	–	–	–	31.6	O06	30	6.8
J1820–0427	B1818–04	25.5	4.7	598.08	84.39(5)	135.9	1.4(5)$\times10^3$	7.8(3.1)	68.58(12)	69.88(14)	285.3	50.3	O05	36	6.8
J1822–4209	–	351.9	–12.8	456.51	72.03(7)	13.3	50(16)	0.63(22)	–	–	–	47.7	O08	76	9.1
J1823+0550	B1821+05	35.0	8.9	752.91	66.83(6)	40.9	1.6(7)$\times10^2$	10(4)	140.99(13)	142.62(14)	17.6	8.9	O07	39	14.7
J1823–3106	B1820–31	2.1	–8.3	284.06	50.225(24)	25.3	1.2(5)$\times10^2$	3.0(1.2)	89.68(9)	90.53(10)	17.5	8.6	O08	30	13.2
J1825–0935	B1822–09	21.4	1.3	769.02	19.34(7)	24.0	2.1(8)$\times10^2$	9(4)	67.61(21)	68.82(22)	25.3	12.8	O05	14	15.9
J1834–0010	B1831–00	30.8	3.7	520.95	89.58(20)	7.6	1.0(5)$\times10^2$	1.2(6)	–	–	–	–	O06	30	13.4
J1834–0426	B1831–04	27.0	1.7	290.11	79.448(25)	82.6	9(4)$\times10^2$	7.7(3.1)	92.35(13)	93.65(14)	85.3	20.7	O05	36	6.7
J1839–0627	–	25.8	–0.3	484.91	92.33(10)	8.1	8(4)e+01	1.5(7)	–	–	–	30.5	O06	30	7.2
J1841+0912	B1839+09	40.1	6.3	381.32	49.143(33)	38.0	9(4)e+01	4.3(1.7)	50.98(28)	52.63(29)	16.8	5.7	O07	60	11.3
J1847–0402	B1844–04	28.9	–0.9	597.81	141.7(7)	22.9	4.6(1.8)$\times10^2$	1.5(7)	–	–	–	385.9	O06	30	9.2
J1848–1952	B1845–19	14.8	–8.3	4308.19	18.0(4)	13.8	9(4)e+01	7.0(2.8)	3.63(20)	4.75(20)†	153.8	76.5	O06	30	7.2
J1849–0636	B1846–06	26.8	–2.5	1451.36	146.7(2.1)	13.4	1.7(7)$\times10^2$	1.2(6)	–	–	–	–	O06	30	6.7
J1851–0053	–	32.1	–0.3	1409.07	24.49(23)	6.5	39(25)	1.8(8)	–	–	–	–	O06	30	12.3
J1900–2600	B1857–26	10.3	–13.5	612.21	37.89(5)	203.6	5.7(1.7)$\times10^2$	19(6)	–8.51(9)	–7.62(11)	48.9	11.4	O08	30	14.7
J1901+0156	B1859+01	35.8	–1.4	288.22	105.459(30)	18.7	9(4)e+01	1.2(5)	–33.52(26)	–31.95(28)†	–	17.8	O07	65	17.3
J1901–0906	–	26.0	–6.4	1781.93	72.47(15)	6.6	27(14)	1.1(5)	–	–	–	39.8	O06	80	6.9
J1909+0007	B1907+00	35.1	–4.0	1016.95	112.58(10)	7.8	77(35)	1.7(7)	–	–	–	47.8	O05	36	10.3
J1909+0254	B1907+02	37.6	–2.7	989.84	171.80(8)	11.8	1.2(5)$\times10^2$	2.2(9)	–	–	–	34.3	O05	36	10.3
J1909+1102	B1907+10	44.8	1.0	283.64	150.012(35)	61.4	3.9(1.6)$\times10^2$	1.7(7)	551.63(18)	553.30(21)	166.0	47.9	O07	80	9.3
J1910–0309	B1907–03	32.3	–5.7	504.61	206.09(23)	16.1	1.6(7)$\times10^2$	1.2(6)	–	–	–	100.2	O05	36	11.5
J1913–0440	B1911–04	31.3	–7.1	825.94	89.34(7)	160.8	5.8(2.3)$\times10^2$	24(10)	3.47(7)	4.68(12)	36.7	13.8	O06	30	8.6
J1916+0951	B1914+09	44.6	–1.0	270.26	61.023(23)	28.8	1.1(5)$\times10^2$	2.0(8)	97.62(17)	99.28(21)	25.0	11.0	O07	80	10.3
J1917+1353	B1915+13	48.3	0.6	194.64	94.718(17)	60.5	1.8(7)$\times10^2$	1.8(7)	227.54(18)	229.26(21)	45.5	15.3	O07	80	7.1
J1919+0021	B1917+00	36.5	–6.2	1272.27	90.12(13)	11.3	47(23)	2.2(9)	–	–	–	42.4	O06	30	13.6
J1921+1948	B1918+19	53.9	2.7	821.04	153.81(9)	20.5	83(34)	0.9(4)	161.7(4)	163.5(5)	–	69.8	O07	80	5.2
J1921+2153	B1919+21	55.8	3.5	1337.30	12.38(11)	539.4	1.8(7)$\times10^2$	9(4)	–17.638(19)	–15.79(13)	41.8	27.5	O07	80	6.2
J1922+2110	B1920+21	55.3	2.9	1077.92	217.07(9)	20.0	71(29)	1.6(7)	–	–	149.9	24.0	O07	80	5.9
J1932+1059	B1929+10	47.4	–3.9	226.52	3.173(19)	304.3	4.8(1.9)$\times10^2$	14(6)	–7.573(8)	–5.90(12)	17.1	4.0	O07	75	9.9
J1935+1616	B1933+16	52.4	–2.1	358.75	158.666(31)	64.2	2.9(1.2)$\times10^2$	4.3(1.7)	–2.04(26)	–0.31(30)	46.4	15.1	O07	40	3.5
J1941+0121	–	39.9	–10.4	217.32	52.21(15)	9.4	71(23)	0.64(25)	–	–	–	24.8	O11	30	3.1
J1943–1237	B1940–12	27.3	–17.2	972.43	28.97(8)	38.6	1.5(5)$\times10^2$	9.6(2.9)	–	–	24.0	12.1	O06	30	2.2
J1944–1750	B1941–17	22.3	–19.4	841.16	56.27(7)	11.4	69(23)	2.6(8)	–	–	47.1	20.3	O06	30	5.4

Continued on next page

Continued from previous page

PSR J	PSR B	l [°]	b [°]	Period [ms]	DM [cm^{-3} pc]	S/N	$S_{\rm mean}$ [mJy]	$S_{\rm p}$ [Jy]	RM$_{\rm obs}$ [rad m^{-2}]	RM$_{\rm IISM}$ [rad m^{-2}]	W_{10} [ms]	W_{50} [ms]	Pointing label	$T_{\rm obs}$ [min]	Offset [°]
J1946+1805	B1944+17	55.3	–3.5	440.62	16.10(7)	19.1	68(28)	0.9(4)	–45.91(30)	–44.14(33)	–	46.1	O07	60	5.9
J1946–2913	B1943–29	11.1	–24.1	959.45	44.26(8)	7.8	34(14)	3.0(9)	3.82(15)	4.69(16)	30.0	9.7	O08	30	13.7
J1949–2524	B1946–25	15.3	–23.4	957.62	23.02(8)	5.3	12(11)	0.83(30)	–	–	–	15.0	O06	30	12.8
J2043+2740	–	70.6	–9.2	96.13	21.041(8)	11.9	47(20)	1.0(4)	–96.88(15)	–95.07(18)	–	4.5	O14	30	10.0
J2046–0421	B2043–04	42.7	–27.4	1546.94	35.89(13)	130.9	78(24)	4.2(1.3)	–2.75(6)	–1.62(16)†	48.5	24.0	O13	59	11.5
J2046+1540	B2044+15	61.1	–16.8	1138.29	39.76(10)	15.2	34(12)	1.8(6)	–90.56(24)	–89.01(26)	68.6	14.2	O14	30	4.4
J2048–1616	B2045–16	30.5	–33.1	1961.58	11.55(17)	430.5	2.6(8)$\times10^2$	9.1(2.7)	–10.450(11)	–9.42(14)	112.0	95.7	O13	71	8.4
J2053–7200	B2048–72	321.9	–35.0	341.34	17.610(29)	70.7	2.1(6)$\times10^2$	5.2(1.6)	18.74(5)	19.37(6)†	42.8	5.8	O12	30	3.1
J2055+2209	B2053+21	67.8	–14.7	815.18	36.40(7)	13.3	28(10)	1.7(5)	–90.08(19)	–88.39(20)	34.8	21.6	O14	30	4.2
J2116+1414	B2113+14	64.5	–23.4	440.15	56.16(4)	9.4	32(11)	0.60(20)	–	–	–	17.0	O14	30	6.2
J2139+2242	–	75.3	–21.9	1083.51	43.87(27)	8.0	28(10)	0.51(18)	–	–	–	90.0	O14	26	9.9
J2155–3118	B2152–31	15.8	–51.6	1030.00	14.90(9)	83.6	68(21)	3.2(1.0)	13.44(4)	14.56(10)†	37.4	24.6	O15	54	12.8
J2253+1516	–	85.3	–38.8	792.24	29.28(7)	8.4	8(5)	0.54(17)	–	–	–	15.4	B05	42	6.6
J2324–6054	B2321–61	320.4	–53.2	2347.49	14.95(21)	10.9	10(4)	0.43(13)	–	–	–	99.6	B09	74	11.4
J2325–0530	–	75.6	–60.2	868.74	14.93(7)	12.3	15(5)	1.17(35)	–	–	17.9	10.2	B04	80	9.6
J2330–2005	B2327–20	49.4	–70.2	1643.62	8.38(14)	192.0	1.3(4)$\times10^2$	8.8(2.6)	9.220(27)	9.97(11)	42.4	25.4	B04	30	8.8
J2336–01	–	84.4	–59.0	1029.80	19.55(9)	23.6	40(12)	1.05(32)	–	–	64.8	36.8	B04	80	12.6
J2346–0609	–	83.8	–64.0	1181.46	22.60(10)	6.5	13(6)	0.78(24)	–	–	–	14.7	B04	30	11.6
J2354–2250	–	48.1	–76.4	558.00	9.97(5)	20.2	12(5)	0.78(24)	9.92(20)	10.72(23)†	27.2	10.6	B07	63	9.7